

**3D DIGITAL METHODS FOR QUANTITATIVE CT-BASED TRABECULAR
VERTEBRAL BONE TEXTURE AND MICROARCHITECTURE ANALYSIS FOR
FRACTURE RISK**

by

Xin Xu

A dissertation submitted to Johns Hopkins University in conformity with the requirements for
the degree of Master of Science in Engineering

Baltimore, Maryland

May 2020

Abstract

There are more than three million cases of osteoporosis in the United States per year, which contributes to two million bone fractures and 19 billion dollars in related expense. The current diagnosis of osteoporosis according to World Health Organization (WHO) criteria is determined by areal bone mineral density (aBMD)--an imaging biomarker examined by dual energy X-ray absorptiometry (DXA) and usually reported as T-score. Nevertheless, many findings suggest that BMD alone is not sufficient to predict fracture risk, and that bone microarchitecture and bone material properties also contribute to overall bone strength.

Due to the difficulty in obtaining high-resolution images on site in-vivo, effective monitoring of bone microarchitecture remains challenging. As a result, osteoporotic drug trials still rely on DXA as well as long-term follow-up to demonstrate fracture reduction, which in turn leads to high expenses and delay of new effective drugs. Currently, there is no diagnosis method in clinical setting that provides both quantitative and qualitative information on bone health, both of which contribute to mechanical bone strength but in distinct ways. New quantitative biomarkers derived from commonly used imaging modalities, e.g. clinical multi-detector CT (MDCT) or micro-CT, could potentially fill that gap. In this work, an ensemble of image-based metrics of bone microarchitecture as candidate surrogate biomarkers of physical properties of bone was systematically evaluated. We established parametric models of bone microarchitecture characteristics to construct intricate realistic 3D trabecular bone structures. This allowed us to build a library of 3D digital trabecular bone phantoms including various bone health levels with established ground truth microarchitecture parameters. The library with a range of bone health

levels spanning from healthy to osteoporotic is essential to ensure better validation and characterization of quantitative performance of the potential biomarkers.

In order to gain a better understanding of the performance of quantitative metrics of bone microarchitecture in relationship to bone strength and to develop an algorithm to construct bone texture structure with specific microarchitecture features, this study involved the analysis of the microarchitecture of 20 healthy L1 vertebrae from donors with age ranging from 44 to 88 years, based on micro-CT scans. 3D digital simulated models of vertebral trabecular bone structure with controlled microarchitecture features were developed to mimic real bone morphology observed from the L1 vertebrae dataset. The same microarchitecture measurement was applied to the simulated models in order to validate the model design algorithm. Furthermore, finite element analysis (FEA) was used to investigate functional physical properties of bone structure with various microarchitecture. Statistical correlation was established between image-based microarchitecture features and physical performance of both the real bone samples and the developed model, to establish a quantitative relation between image-based metrics and corresponding physical features.

This investigation provides evidence that microarchitecture contributes substantially to bone strength along with BMD. The model established in this study can generate phantoms with desired microarchitecture measurements within 5% error on each parameter. The capability of the designed model to generate bone structures with high variability and complexity is an aid in further discovery of potential quantitative image biomarker for fracture risk prediction.

Primary Reader and Advisor: Wojciech Zbijewski

Secondary Readers: Kendall Moseley, Alejandro Sisniega

Acknowledgments

Many thanks to Dr. Qin Li, Dr. Nicholas Patrick, Quantitative Imaging team of DIDSR, US FDA, ORISE, OWH, for the generous funding and the assistance with this project.

I am also grateful to Professor Wojciech Zbijewski as my academic PI, for his kindness, support for the thesis. Also, Dr. Sina Youssefian was being very helpful as I progressed my project. Additionally, I need to thank Dr. Kendall F. Moseley and Dr. Alejandro Sisniega as my thesis readers to provide invaluable advice on modification and improvement.

Table of Contents

Abstract	iii
Acknowledgments	v
List of Tables	viii
List of Figures	ix
Chapter I Introduction	
Background of the Problem	1
Question and Hypothesis	16
Implication of Research	17
Chapter II Materials and Methods	
Real Bone Specimen Data	20
3D Digital Phantom Development	21
Characterization of the Structure Network	22
Morphological Processing	27
Model Validation	31
Microarchitecture Analysis	32
Finite Element Analysis	36
Statistical Analysis	38
Chapter III Results	
Graphical 2D and 3D Visualization	40
Microarchitecture Features	43
Mechanical Property	54

Chapter IV Discussions and Conclusion

Discussions on the results 57

Conclusion 59

Chapter V References

Resources and References 62

Curriculum Vitae 71

List of Tables

Table 1	Osteoporosis diagnostic guidelines	5
Table 2	List of microarchitecture measurements.....	32
Table 3	Look-up table of 375 simulated models	44
Table 4	Microarchitecture measurements of the structures in Figure 36.....	49
Table 5	Microarchitecture measurements of the structures in Figure 37.....	49
Table 6	Microarchitecture measurements of the structures in Figure 38.....	50
Table 7	Microarchitecture measurements of the structures in Figure 39.....	50
Table 8	Microarchitecture measurements of the structures in Figure 40.....	51
Table 9	Microarchitecture measurements of the structures in Figure 41.....	52
Table 10	Microarchitecture measurements of the structures in Figure 42.....	52
Table 11	Microarchitecture features and physical properties of four structures.....	54
Table 12	Improvement on the physical property performance with consideration of matching standard deviation values	55
Table 13	Comparison of the parameters of four pairs of real bone and corresponding digital phantom.....	56

List of Figures

Figure 1	An example of a vertebral trabecular bone.....	3
Figure 2	Distribution of BMD in young healthy women.....	6
Figure 3	Distribution of BMD in women at different ages.....	7
Figure 4	Sample HR-pQCT images	11
Figure 5	MDCT image of a proximal femur	12
Figure 6	CBCT scan of a cadaver foot	13
Figure 7	A distal tibia acquired in MRI and HR-pQCT.....	13
Figure 8	An example of trabecular bone score computation.....	14
Figure 9	Process of generating trabecular bone-like structure.....	22
Figure 10	Illustration of seed-point distribution setting	23
Figure 11	Illustration of Centroidal Voronoi Tessellation	24
Figure 12	A vertebral bone from a young individual	24
Figure 13	Illustration of the flow along z-direction in this study.....	25
Figure 14	Process of seed-points distribution	26
Figure 15	Simulated bone structures with different generating parameters	27
Figure 16	A fully connected network before edge pruning.....	28
Figure 17	One of the Voronoi cell formed by the network.....	28
Figure 18	Illustration of definition of plate and rod orientation.....	29
Figure 19	Process of obtaining a simulated trabecular bone structure	30
Figure 20	Example of a Gaussian distributed variation factor matrix.....	31

Figure 21	Thickness map of trabecular thickness and trabecular spacing.....	34
Figure 22	Steps of image processing prior to BoneJ measurement.....	36
Figure 23	Illustration of the definition of stiffness and modulus.....	36
Figure 24	Real bone structure in mesh.....	37
Figure 25	A visualization of the output of Abaqus.....	38
Figure 26	Steps of digital phantom development.....	40
Figure 27	3D visualization of a real bone and a digital model.....	41
Figure 28	A real bone structure and its corresponding digital phantom with bone volume fraction about 0.2.....	41
Figure 29	Distance map of a selected slice of a real bone and a corresponding digital phantom.....	43
Figure 30	Visualization of the correlation using correlogram.....	45
Figure 31	Boxplots of bone volume ratio and trabecular spacing.....	45
Figure 32	Boxplots of measured trabecular thickness to the input trabecular spacing.....	46
Figure 33	Boxplot of connectivity density to the input trabecular spacing.....	47
Figure 34	Boxplot of input randR to measured degree of anisotropy.....	47
Figure 35	Boxplot of input randR to measured degree of anisotropy at certain levels of input bone volume fraction.....	48
Figure 36	VOI extracted from patient 05751 and corresponding simulated structure.....	49
Figure 37	VOI extracted from patient 04216 and corresponding	

	simulated structure.....	49
Figure 38	VOI extracted from patient 06219 and corresponding simulated structure.....	49
Figure 39	VOI extracted from patient 14-0120 and corresponding simulated structure.....	49
Figure 40	VOI extracted from patient 05880 and corresponding simulated structure.....	49
Figure 41	VOI extracted from patient 06604 and corresponding simulated structure.....	49
Figure 42	VOI extracted from patient 04216 and adjusted corresponding simulated structure.....	52
Figure 43	Histogram of degree of anisotropy.....	53
Figure 44	Visualization of the distribution of the parameters of the four pairs.....	56
Figure 45	3D printed bone structures.....	61
Figure 46	Simulated projection of a digital spine phantom.....	61

Chapter I

Introduction

Background of the Problem

Bone is a dense connective tissue that is ever-changing throughout the lifecycle. Bone is continually created and replaced in a process called remodeling. A remodeling cycle requires the removal of mature bone tissue in a process called bone resorption with subsequent formation of new bone tissue by ossification. During early stage of one's life (childhood and teenage years), new bone is formed faster than mature bone is removed, and so bones grow denser along the time. However, once peak bone mass with maximum bone strength and density is reached, a steady state of bone remodeling eventually transitions to one in which bone resorption outpaces formation. In women, this occurs during the perimenopausal transition. In men, bone loss predominates around the seventh decade of life. If the bone lost exceeds that of the normal population, osteoporosis may occur (NIH, 2018). Osteoporosis, a disease that is characterized by low bone mass, low bone mineral density, and structural deterioration, is the most common cause of bone fractures among the elderly as aging is one of the major risk factors for osteoporosis (Britton, et al., 2010). More than three million fractures occur yearly in the US (Mayo Clinic, 2019), and 15 million cases occur worldwide per year. Osteoporosis and its sequelae are responsible for \$19 billion in related health care costs every year (F. Cosman, et al., 2014), and thus it becomes one of the most substantial public health challenges given the aging of the population.

As mentioned above, the fundamental mechanism of osteoporosis development is the imbalance between bone resorption and bone formation. In healthy bone, remodeling occurs at a constant rate, and at any point of time, there may be up to 10% of all bone mass undergoing remodeling (H. John, 2010). These osteodynamics are controlled in the cellular and molecular level. Two main types of cells are involved in bone metabolism: osteoclasts degrade the bone matrix (bone resorption), releasing minerals and signaling factors into the blood; recruited to sites of active resorption, the osteoblasts rebuild the bone matrix by depositing osteoid which will mineralize in time to form new bone (H. Frost, et al., 1963). The activity of osteoblasts and osteoclasts are signaled by a bunch of chemical enzymes that can promote or inhibit certain actions of the cells (L. Raisz, et al., 2005). The bone remodeling cells can also control the activity of each other by paracrine signaling.

Within any individual bone, the bone tissue can be divided into two main structures based on the characteristics and appearance, which are the cortical and trabecular bone. Trabecular bone is the porous bone in the vertebrae and the ends of long bones such as the femur; while cortical bone is the concrete outer shell of bones. Given its porous structure, trabecular bone has larger overall surface area than cortical bone and is more active and subject to more bone remodeling. Given the higher remodeling rates of trabecular bone, microarchitectural deterioration is most pronounced in sites that have relatively high trabecular to cortical bone ratio like lumbar spine and femur bones (NIH, 2018). Those areas rely heavily on the trabecular bone for strength, and so are more likely to degenerate when bone resorption and formation are imbalanced. Figure 1 shows an illustration on vertebral trabecular bone structure.

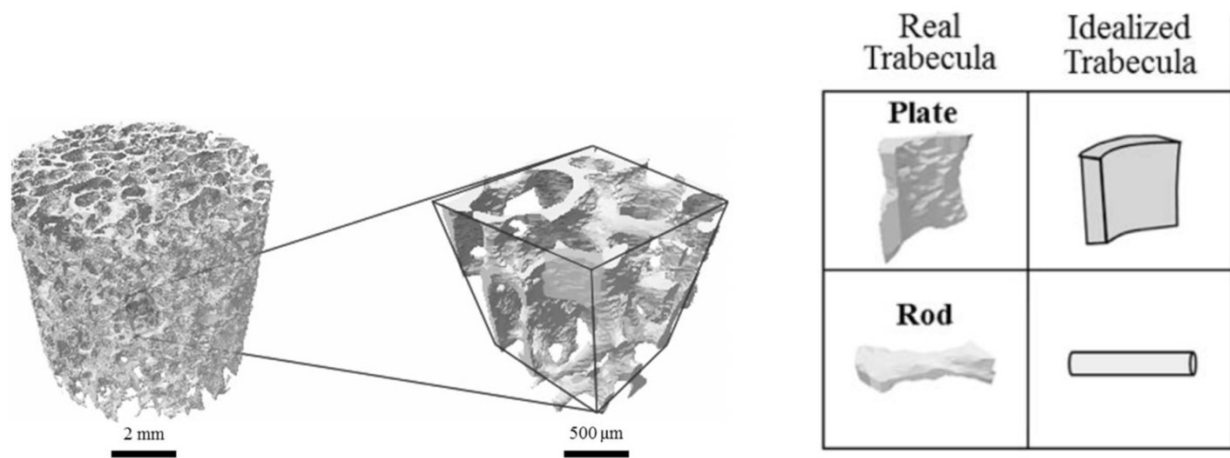


Figure 1. An example of a vertebral trabecular bone specimen at the left and a scale-up version of part of the vertebra to show details of rod-like and plate-like structures in the middle. The right shows schematic representations of trabecular structures as rod and plate.

Osteoporosis shows as not only decreases in bone density but also microarchitecture disruption. Both bone quantity and bone quality contribute fundamentally to bone strength, and the decrease in bone density and microarchitecture deterioration can be seen as decline in bone quantity and in bone quality. Although both affect bone strength, quantity, (estimated by bone mineral density) and quality, (which can be assessed by microarchitecture features) are not necessarily at the same state in all cases. Literature shows instances where equivalent bone density was measured in subjects with distinct outcomes in bone fractures (A. Warriner, et al., 2011). Thus, investigation on tissue structure of the bone is as essential as bone mass estimation for fracture risk prediction.

Although bone mass and bone strength decline with aging, osteoporosis may occur due to the imbalance or abnormal level of specific hormones--e.g. lower levels of estrogen. Chronic diseases and therapeutics used to treat them may also lead to osteoporosis. Kidney diseases,

hyperthyroidism, anorexia nervosa, and alcoholism are some common diseases that may cause osteoporosis; medications including, antiseizure medicine, chemotherapy, and glucocorticosteroids may increase the bone loss rate and lead to osteoporosis (NIH, 2018). While there are many risk factors that are either iatrogenic or modifiable, there are a number of nonmodifiable risk factors that equally contribute to osteoporosis and fracture risk .

Sex is one of the top risk factors of osteoporosis; among all cases in U.S., about 80% of patients are women, not only because of the higher prevalence and rate of fracture than men, but also difference on other bone characteristics between sexes (National Osteoporosis Foundation, 2018). Literature has revealed gender difference in bone sizes, microarchitecture and the mechanism of bone density loss in a microstructural level. With pair groups of men and women matched for age, weight, vertebral bone density, and vertebral body height, research shows that women have overall cross-sectional areas of vertebral volumes 25% smaller than men, though the difference of vertebral bone densities between sexes is not statistically significant (V. Gilsanz, et al., 1994). F. Eckstein et al. suggests that the sex differences of trabecular bone microstructure are site dependent. At the radius and femoral neck, men have trabecular bone with significantly more plate-like structure, smaller trabecular separation (Tb. Sp.), but higher in trabecular thickness (Tb. Th.), connectivity density (Conn. D.) and degree of anisotropy (D. A.) compared to women. At the trochanter, men also show more plate-like structure and higher Tb. Th. than women, but no significant difference in Tb. Sp. or other parameters. At the calcaneus, gender difference is not shown on any of the parameters (F. Eckstein, et al., 2007). M. Hudelmaier, et al. also reported significantly lower bone mineral density (BMD), bone volume fraction (BVF), and Tb. Th. in women when compared to men, which indicates lower bone quality (M. Hudelmaier, et al., 2005).

Ethnicity is another important risk factor in bone health. According to the statistics provided by National Institute of Arthritis and Musculoskeletal and Skin Disease, white and Asian are at greater risk and African American and Hispanics have a lower but still in a significant risk than other ethnic groups (NIH, 2018). Family history of fractures may also contribute to reduced bone mass and may be sign of risk for fracture, as the heritability of fracture and low bone mineral density ranges from 25 % to 80%, and there are more than 30 genes associated with osteoporosis development (L. Raisz, et al., 2005). F. Ojo, et al. suggest that subjects who had a fracture previously are at least twice as likely to develop osteoporosis later in their life compared to individuals of the same age and sex who do not have a history of bone fractures (F. Ojo, et al., 2007). Results in (B. Alldredge, et al., 2009) point to greater risk of osteoporosis for individuals of small body size with thin bones.

In the absence of an osteoporotic fracture, the current diagnosis of osteoporosis is made by measuring BMD on DXA according to the standard defined by World Health Organization as shown in Table 1 (WHO, 2003). The major clinical imaging modality for BMD measurement is dual-energy X-ray absorptiometry (DXA), DXA is a spectral imaging technique that uses two X-ray beams at different energy levels. A weighted combination of the different X-ray absorption from the two beams is then computed to remove the contribution of soft-tissue to the measurement, yielding an estimation of the absorption attributable to bone only (National Osteoporosis Society, 2018). DXA is currently considered the gold standard for osteoporosis diagnosis, and the BMD measurement taken from DXA can be transformed into T-score as a quantitative biomarker. WHO has provided the guidance for osteoporosis diagnosis based on bone density in women and men by following four general diagnostic categories (WHO, 2003): normal for BMD values within 1 standard deviation (SD) of the young adult reference mean (T-score of -1.0 or above); osteopenia,

or low bone mass, for BMD values more than 1 SD but less than 2 SD below the young adult mean (T-score between -1.0 and -2.5); osteoporosis for BMD values 2.5 SD or more below the young adult mean (T-score below -2.5); established osteoporosis, or severe osteoporosis for BMD values 2.5 SD or more below the young adult mean with one or more fragility fractures.

Category	BMD	T-score	Percentage of Population
Normal	BMD > mean-SD	T-score \geq -1	85%
Osteopenia	mean-SD > BMD > mean-2SD	-1 < T-score < -2.5	14%
Osteoporosis	mean-2.5SD > BMD	T-score \leq -2.5	0.6%
Established Osteoporosis	mean-2.5SD > BMD with fragility fracture	T-score \leq -2.5 with fragility fracture	< 0.4%

Table 1. Osteoporosis diagnostic guidelines provided by WHO.

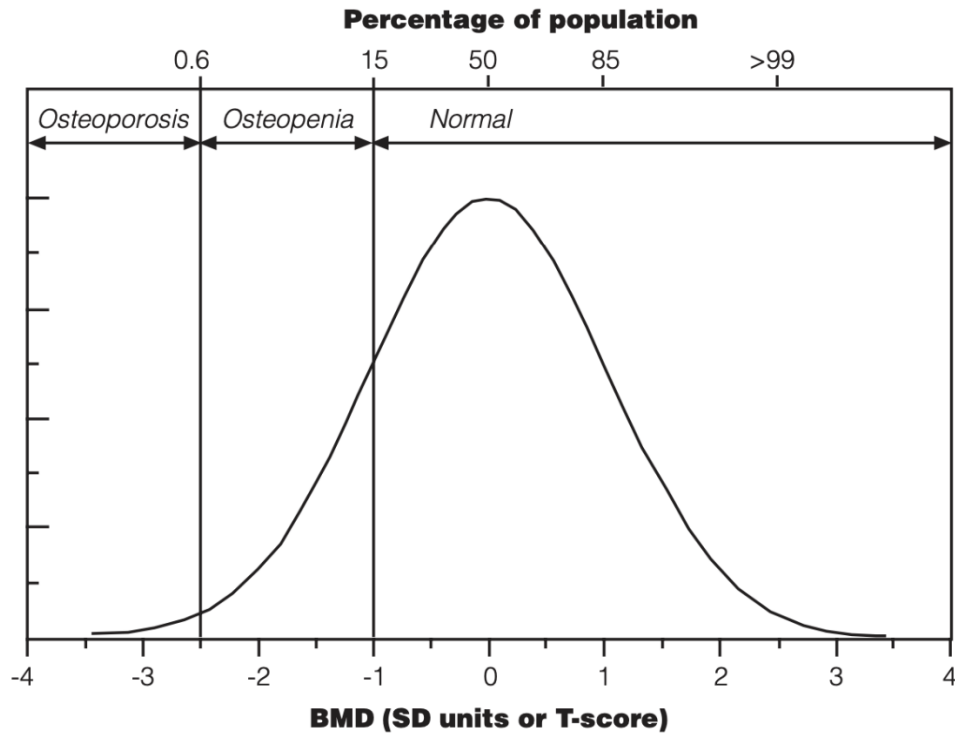


Figure 2. Distribution of BMD in young healthy women aged 30-40 years. Bone mineral density in the population follows a normal distribution from statistics collected by WHO (WHO, 2003).

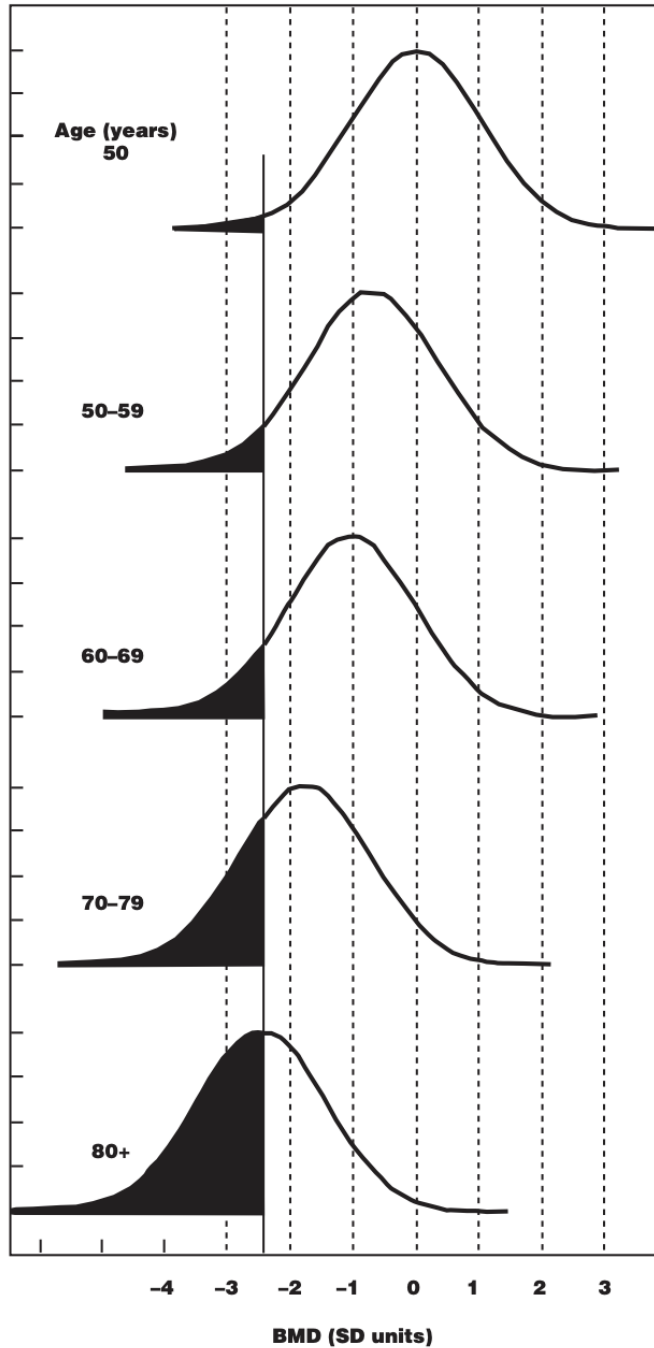


Figure 3. Distribution of BMD in women at different ages from WHO dataset.

As is shown in figure 2 (WHO, 2003), BMD is normally distributed in the population, and so in the young healthy population, approximately 15% will have a T-score value less than -1 which indicates low bone mass or say osteopenia, and about 0.6% are with T-score of -2.5 or lower and thus meeting the criteria for osteoporosis. From figure 3 (WHO, 2003), BMD at all ages is normally distributed, but the mean value of the normal distribution decrease progressively as age increases; in other words, the proportion of women with osteoporosis increases markedly with age and so does the fracture risk. Moreover, the prevalence of osteoporosis increases exponentially and is in line with the increasing fragility fractures among ageing women. WHO does not provide enough investigation to draw concrete conclusions for men or other ethnic groups. However, small population studies have shown that the cut-off BMD values used in women can be used for osteoporosis diagnosis in men as well, although the threshold value may need appropriate adjustment based on body size in some populations (WHO, 2003).

The standard DXA scan is a two-dimensional projection which yields a measurement of areal BMD (aBMD) in units of g/cm^2 , rather than the real bone mineral density which should be in unit of g/cm^3 . The confounding effect of differences in bone size may lead to inaccurate estimation of BMD as the area and volume are not in a linear relationship. In another hand, the error of actual bone size due to the missing depth value may actually improve the BMD value since bone size is another determinant of bone strength. This inaccuracy appears particularly common at the spine since vertebral bone are irregular both in shape and apparent density, and the measurements also partly depend on the applied edge detection algorithm. This shortcoming can however be mitigated by estimating the volume from the projected area measured by DXA, and the adjusted result is referred as bone mineral apparent density (BMAD) with the same units as volumetric BMD. Nevertheless, BMAD still lacks the ability of accurately represent the true BMD

since the bone volume is approximated instead of directly measured, and so BMAD is not currently used in the clinical practice (WHO, 2003).

BMD alone does not fully capture fracture risk or provide accurate assessment for many patients who are at risk without other biological markers and clinical factors. While BMD gives an absolute risk indication, the FRAX® algorithm used by WHO is a relative risk predictor that includes more possible risk factors, such as gender, and it is used to predict 10-year fracture risk in a given patient (J.A. Kanis, et al., 2011). However, it is not yet been used in FDA's decision-making for any bone drug trial.

Bone Structure in Interpretation of Bone Strength

Moreover, except the lack of calibration based on risk factors, BMD is also restricted in incorporating enough information on bone quality that can be represented by microarchitecture features, and only provides a quantity measurement of bone mass in terms of bone mineral density. Loss of bone can be represented by bone mass loss as well as significant skeletal microarchitecture deterioration, and the collective changes in both bone mass and microstructure lead to decreased bone strength with increased fracture risk (G. Diederichs, et al., 2009). Bone strength prediction can be improved with BMD measures in combination with trabecular microarchitecture measurement, as bone mass with same quantity may exhibit various bone structures perform mechanically resistance differently. Indeed, bone loss and bone microstructure changes happen in parallel with one another. Bone loss directly leads to decreased number of trabeculae (Tb. N.), increased Tb. Sp., and loss of Conn. D. of the trabecular bone matrix (F. Eckstein, et al., 2007). Deterioration of microarchitecture will lead to compromised bone strength.

Historically, bone biopsy provided a good assessment of bone microarchitecture properties ; however, it is an invasive procedure that cannot be done easily or at the bedside. Biopsies are typically obtained from the iliac crest, a non- weight-bearing site. Moreover, bone biopsy is unable to assess changes in longitudinal direction accurately since selected sites vary in different cases. Lumbar spine and femur are the most commonly used sites for response monitoring of osteoporosis drugs. However, due to the slow remodeling rate of bone that can hardly be captured by DXA to investigate bone loss instantly, as well as the lack of effective way to obtain high-resolution 3D images of those sites in-vivo to better investigate the role that bone microarchitecture plays in bone mechanical strength, osteoporotic drugs trials still depend on long-term follow-up of patients by counting the number of fracture incidences between the treatment and control groups (T.M. Link, 2012). As a result, the lengthy drug trials are extremely inefficient because of the expensive costs and delay of the introduction of potential effective treatment for at-risk patients. Innovative biomarkers which can accurately and efficiently predict fracture risk are needed.

Recent developments in imaging techniques provide the possibility to better investigate bone microarchitecture, an important determinant of bone strength, in a higher resolution. High-resolution peripheral quantitative computerized tomography (HR-pQCT) imaging has overcome some of the limitations mentioned above. HR-pQCT imaging can be seen as noninvasive bone biopsy providing assessment of bone geometry in vivo with extremely high resolution (up to 60 to 82 μm) with low radiation when it is limited to sites at the distal radius and tibia only (A. Cheung, et al., 2013)--effective dose for HR-pQCT is lower than 0.003 mSv (M. Burrows, et al., 2010), for imaging of distal tibia in adolescents (XtremeCT, scanco), comparing to a 0.013 mSv effective dose for spine radiographs using fan-beam DXA (J. Damilakis, et al., 2010). As shown in Figure 4 (K. Roland, et al., 2011), the high resolution of HR-pQCT permits the ability to display the bone

microarchitecture and reconstruct the scans in to a 3D visualization. HR-pQCT differs from DXA in that it is possible to measure volumetric bone mineral density in vivo and reconstruct bone microarchitecture in 3D. Moreover, bone mechanical properties can be estimated with Finite Element Analysis on the HR-pQCT images (A. Cheung, et al., 2013). Nevertheless, pQCT only assesses two bone sites as mentioned, and hence whether measurements at those sites can accurately reflect strength at the axial skeleton remains a concern. Furthermore, although HR-pQCT can achieve the highest resolution among all in vivo imaging modalities, human trabeculae have physical dimensions comparable to the system resolution, which may hamper accurate segmentation of fine details in the bone trabecular structure. HR-pQCT is still mainly used in research investigation, and it has not yet received FDA regulatory approval for clinical use.

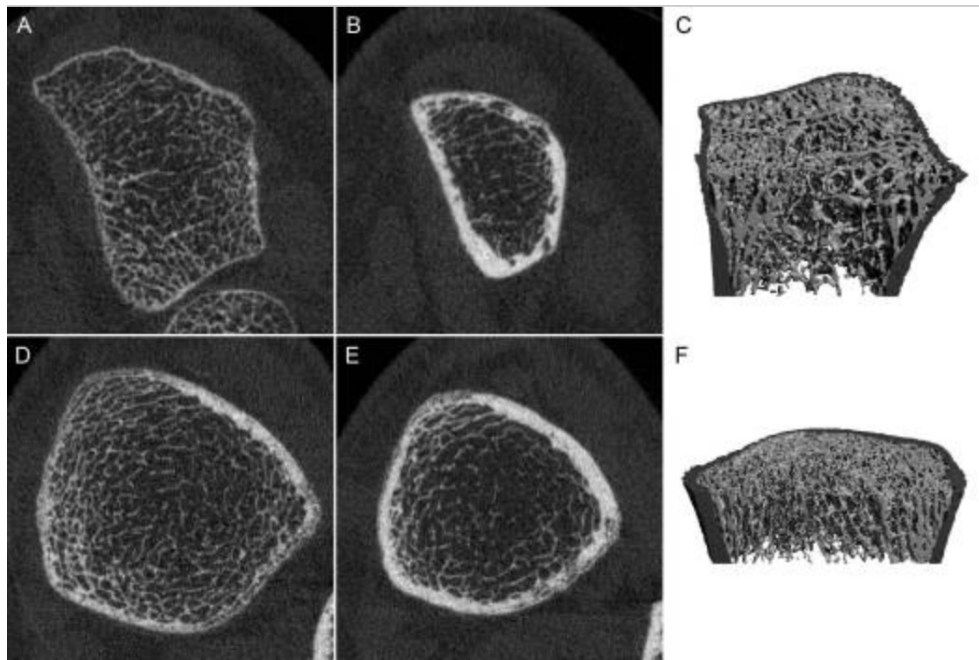


Figure 4 (K. Roland, et al., 2011). Sample HR-pQCT images from (A-C) distal radius and (D-F) distal tibia where (A) and (D) are the distal most slices of the scan, (B) and (E) are the proximal most slices of the scan, and (C) and (F) are the 3D reconstruction visualization of the segmented bone structure with the dark gray representing cortical compartment.

Another modality with high resolution but more clinically available, high resolution multi-detector computed tomography (MDCT), uses a two-dimensional detector array to acquire multiple slices simultaneously (K. Mei, et al., 2017). The introduction of multiple rows of detectors not only increases the imaging speed but also the imaging length, which will increase the patient effective dose by z-overscanning. Z-overscanning refers to the tissue extent that is exposed to x-ray beyond the boundaries of target volume of interest to reconstruct the first and last slices with additional rotations (A. Tzedakis, et al., 2005). As a result, MDCT is limited in the use of osteoporosis diagnosis due to its relatively high radiation exposure caused by z-overscanning effect (J. Damilakis, et al., 2010), as the effective dose of approximately 3 mSv to examine vertebral microarchitecture comparing to 0.06-0.3 mSv for 2D spine QCT scan. Figure 5 shows a single slice of MDCT scan with an osteoporotic right intertrochanteric fracture. Note that the high noise level inhibits the image to provide a good view of individual bone trabeculae but more of a texture of the region. Cone-beam computed tomography (CBCT) is widely used in dental settings and also other applications, e.g. extremities imaging, image-guided radiation therapy, but there were a few studies used CBCT technique to evaluate osteoporosis at the jaw (E. Güngör, et al., 2016). CBCT for osteoporosis diagnosis may need extra cost by special phantoms and additional programs required (C. Brasileiro, et al., 2017). Additionally, studies show that CBCT-derived quantitative radio-morphometric indices are limited in screening individuals with low BMD due to the lack of standardized study with larger sample size and calibration on technical parameters of the scans (such as voxel size and tube voltage and amperage) which significantly affect the image quality and measurements (E. Guerra, et al., 2017). Figure 6 shows axial and sagittal views of a CBCT volume of a foot (M. Posadzy, et al., 2018). The high spatial resolution of CBCT provides the ability to investigate bone microarchitecture in an exquisite way as shown in Figure 6, however,

the potential use of CBCT in osteoporosis still need further studies with more promising results to establish standard guidelines (E. Guerra, et al., 2017). High-resolution magnetic resonance (HRMR) is another possible imaging modality that is clinically accessible and can provide 3D volumetric microarchitecture information. Although technological development permits quantitative MRI to be more clinically practical in use of bone structure analysis, spatial resolution and signal to noise ratio (SNR) of MRI scans for deep body location can only be improved by high magnetic field strength (R. Krug, et al., 2011). Figure 7 shows the same distal tibia acquired on an MRI system and on a HR-pQCT. Note that HR-pQCT provides higher image resolution yielding better visualization of the bone microarchitecture.

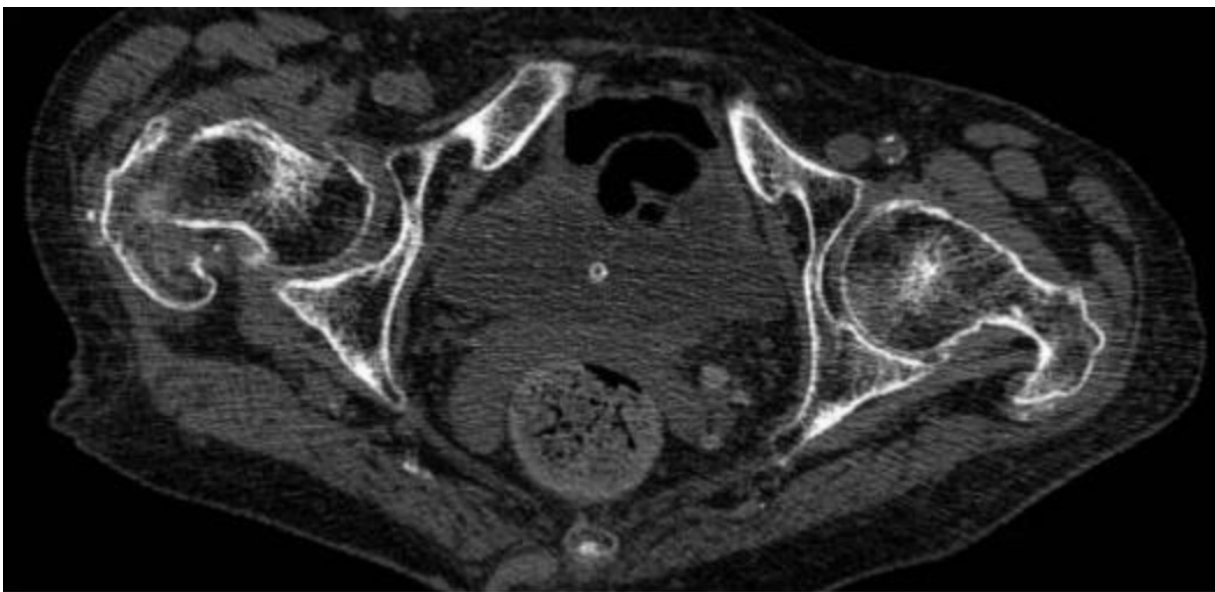


Figure 5 (R. Krug, et al., 2011). MDCT image of a proximal femur. The imaging setting is 120 kVp, automatic current modulation at 70 to 500 mA, noise index of 50, reconstructed at 1.25 mm with slice thickness of 0.625 mm.

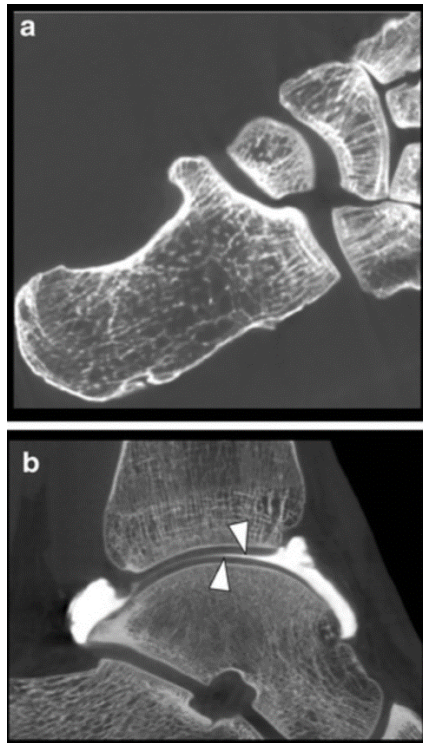


Figure 6 (M. Posadzy, et al., 2018). CBCT scan of a cadaver foot in (a) axial image that shows detailed cortical and trabecular bone microarchitecture; (b) reformatted sagittal image of the talocrural joint after intra-articular contrast injection to show the smooth surface of articular cartilage.

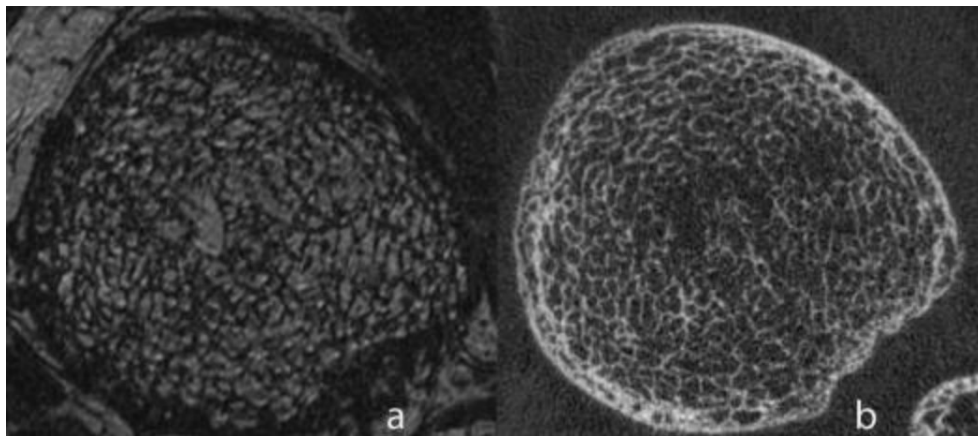


Figure 7 (J. Goldenstein, et al., 2010). A distal tibia acquired in (a) MRI at 3 Tesla, and (b) HR-pQCT.

Quantitative Measurement on Bone Microarchitecture

Despite the ongoing investigation on potential use of the high-resolution imaging techniques, trabecular bone score (TBS) is a bone texture measurement introduced in 2008, which is correlated with bone microarchitecture and as a biomarker for osteoporosis prediction used widely in research field (L. Pothuaud, et al., 2008). TBS is a grey-level texture measurement that utilizes experimental variograms in anteroposterior DXA scans of lumbar spine to reflect bone microarchitecture and to provide additional skeletal information that is missing from BMD measurement, where variogram is computed by the sum of the squared gray-level intensity differences between pixels at a set distance. Figure 8 shows an example of TBS computation in a simplified illustration (B. Silva, et al., 2014). Significant correlation was found between the microarchitecture characteristics of trabecular bone (BVF and Tb. Th.) obtained from 3D micro-computed tomography (μ CT) reconstruction and the TBS evaluated by the 2D projection derived directly from the 3D μ CT images (L. Pothuaud, et al., 2008). TBS was initially calculated from 3D μ CT and later adapted directly on DXA images which is the routine clinical practice for osteoporosis diagnosis.

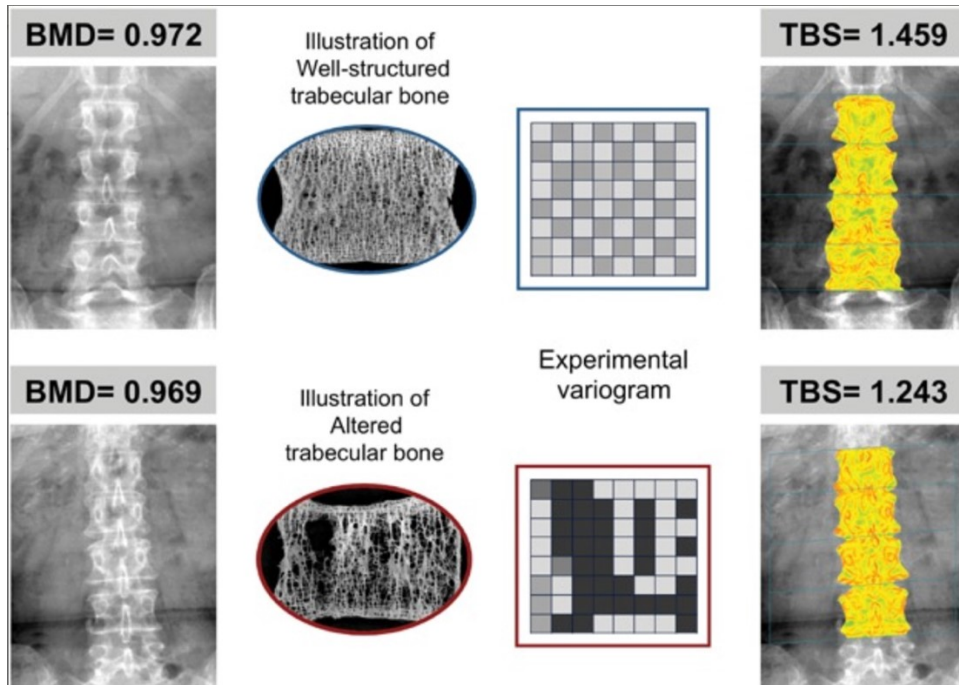


Figure 8 (B. Silva, et al., 2014). An example of trabecular bone score computation. TBS is the number of filled voxels versus the number of unfilled ones based on the experimental variogram, that means more in quantity and connectivity, but less sparse trabeculae yield to higher TBS value; while less numerous and connected structure, but more trabecular separation will lead to lower TBS. Besides, the pair shows structure can have similar BMD but different TBS which indicates the independency of TBS to BMD and inadequacy of BMD alone to predict fracture risk.

The 3D characterization of bone microstructure provided by high resolution imaging techniques allows the introduction of novel radiometric to render assessment of bone microarchitecture, however, only a few of studies were conducted to investigate the quantitative performance of bone microarchitecture and bone texture features among the imaging techniques mentioned above. Legrand et al. have conducted a research on the correlation between BMD and vertebral fragility fractures (E. Legrand, et al., 2000). Lumbar BMD was assessed with DXA, and a set of bone structure parameters were computed with X-ray films from pair groups of healthy subjects and bone fracture patients. The metrics included in the study were: BVF, Tb. Th., Tb. N., Tb. Sp., and Conn. D. (degree of fragmentation of the trabecular network). With adjusted level of BMD, no significant differences were found between the two groups in terms of bone volume

fraction, and average thickness. Connectivity, and trabecular spacing are significantly higher in patients with fractures, while trabecular number is lower.

Lowitz et al. compared BMD and trabecular microarchitecture using MDCT and HR-pQCT to investigate the impact of different imaging modalities (T. Lowitz, et al., 2017). In the study, they found good linear correlation in microarchitecture and texture measurements between the two modalities, but the results were heavily dependent on image resolution. Guggenbuhl et al. showed that CT-based bone texture measurements are influenced by the reconstruction slice thickness and so implying the significance of the conditions of acquisition for reproducibility of the parameters (P. Guggenbuhl et al. 2008). Diederichs et al. assessed trabecular microarchitecture parameters derived from MDCT, and established correlation to those obtained with μ CT, and biomechanical testing of bone strength (G. Diederichs, et al., 2009). Results showed significant correlation between parameters derived by MDCT and μ CT, and the combination of those parameters with additional texture index, the prediction of mechanical bone strength are highly improved from using single measurement.

The noted studies all show the feasibility of multivariate models of BMD, structural parameter, or texture measurements that combined can improve the prediction of physical bone strength, and suggest a more reliable estimation of fracture risk over time. However, the studies above were limited to small sample size or even none of healthy bones due to the inaccessibility to young healthy subjects, since patients who underwent such scans are usually already affected by bone fractures or osteoporosis. Additionally, due to limitations of each particular imaging modality, such as low signal to noise ratio, motion artifacts, and high dose, etc., the impact of many

other image acquisition parameters was not evaluated, and a solid conclusion cannot be drawn yet due to the limited data.

Question and Hypothesis

The purpose of this study is to develop a morphologically and mechanically realistic digital phantom to provide a wider range of data to evaluate the quantitative performance of microarchitecture features in prediction of mechanical competence. These data will aid in development of surrogate biomarkers to assess fracture risk and treatment response for use in drug trials and therapy monitoring.

In order to develop a realistic phantom, human data was assessed in a designed pipeline that is the same as the one applied to designed phantoms, to guarantee consistency of the measurement results; as shown in previous studies, different image processing algorithms will lead to different results. Moreover, morphological characteristics should be measured and summarized to produce similar structure. In this study, the phantom development focused on the lumbar spine, a site frequently used for monitoring the response of osteoporosis drugs. The resulting digital phantom development algorithm should have the ability to include various levels of bone health, and the ground truth of bone microarchitecture parameters should be evaluated and included in the phantom specifications. Last but not the least, it should have morphological and physical properties in agreement with the ones informed by human dataset and literature.

The hypothesis of the study is that when a corresponding digital phantom is developed with all microarchitecture features match with a selected human sample, their physical behavior should

be similar within certain range. Once the realistic phantom is developed, a library of public digital phantoms can be implemented with the distribution of each microarchitecture parameter the same as the distribution of the human data. Additionally, analysis on the physical performance with varying microarchitecture features will be investigated as well.

Implication of Research

Clinical evaluation, diagnosis and management of osteoporosis is performed using dual-energy X-ray absorptiometry. There are more than 140 bone densitometry 510(k) pre-market submissions to the FDA as for osteoporosis diagnosis. However, there is a lack of an effective approach approved by FDA for clinical use to characterize bone microarchitecture quantitatively despite the fact that many studies have shown the significant role that bone structure deterioration plays in osteoporosis development. Therefore, clinical trials for osteoporosis drug pre-market approval are lengthy and costly as they require both changes in BMD and fracture endpoints to show therapeutic efficacy.

The development of digital phantoms realistically depicting bone trabecular structure can be a potential tool for the development and evaluation of imaging-based devices and tools for characterization of trabecular bone. Digital trabecular bone models were built in MATLAB, and the developed code will be publicly available for reproducibility of trabecular bone phantoms with known ground truth of the synthetic bone parameters. Recommendation on parameter selection for different bone health level and sites will be included as well. A library of 3D digital phantoms for texture analysis or any other image-based assessments will be publicly available. The library will

cover a broad range of bone health levels.. The pipeline for the digital phantom development ensures that the properties of the simulated structures, according to the desired bone health level, will be well-controlled and correlated with bone strength. As a result, these phantoms are available for comprehensive technical assessment of quantitative measurements providing a well characterized ground truth and well-controlled levels of bone health, providing the possibility for bias and linearity analysis. This kind of quantitative analysis is not always possible in actual patient data due to the limited availability of such data, especially for repeatability and reproducibility analysis. Additionally, high dose, high-resolution scans, and μ CT scans of bone biopsies provide a good ground truth for phantom design, while they are either not practically usable in clinical scenarios.

This study aids in determination of which image-based microarchitecture features can robustly measure physical properties of bone and serve as potential biomarkers in bone health drug trials. Such information may be beyond currently available options approved for standard-of care DXA. Many follow-up applications can be used with the developed phantom. The human data used in the study is acquired from μ CT, and so the phantoms developed mimic the morphological characteristics of human bone as measured with μ CT. The bone structure phantoms can be used to evaluate a wide range of imaging settings, including spatial resolution, reconstruction kernel, noise level, etc. Simulation are not limited to μ CT images since the phantoms are generic enough to be used in any other possible image modality. Moreover, 3D printed physical phantoms based on the developed phantom models can be produced by using representative parameters. The 3D printed phantoms can then be physically scanned in an imaging modality to validate the simulated measurements.

Chapter II

Materials and Methods

Real Bone Specimen Data

The human data source is from Dr. Vivek Palepu, a staff fellow from Center of Devices and Radiology Health in the U.S. Food and Drug Administration. The study pool included 104 patients. All the patients are white with age 44 year as minimum, 98 years as maximum, and 76 years as median; and 65 of them are females, and 39 of them are males. Vertebral bone specimens from the patients were taken from one of the following sites: T7, T8, T9, T12, L1, L2, L3, L4, L5, or any combination of them. The bone specimens were scanned on a μ CT scanner (SCANCO Medical) and saved in DICOM format as image sequences. The μ CT acquisition protocol involved a voltage of 70 kVp with 0.5 mm Al filtration, and x-ray exposure of 80 μ As with 400 s total exposure time. The slice thickness was 0.0513 mm (51.3 μ m), and the pixel size was equal to the slice thickness (isotropic) 0.0513 x 0.0513 mm², equivalent to a resolution of 19.4933 pixels per mm. The bone microarchitecture measurements for each bone specimen as a whole were computed with SCANCO_V1.2a, a built-in software of the SCANCO μ CT scanner. Additionally, bone mineral density was reported as T-score in some of the patients' record. Although the full statistics of the 104 patients were in file, to ensure reproducibility and consistency of the data, image processing and microarchitecture measurements on the μ CT images were conducted in a set pipeline, which will be discussed in detail later. In this study specifically, 20 L1 vertebral bone specimens were selected from the full 104 patients dataset. Measurements were performed on a volume of interest (VOI) of 200 x 200 x 200 pixels (10.26 μ m³), and for each bone specimen, 20

VOIs were extracted from partially overlapping regions. As a result, 400 VOIs were collected in the final human control dataset, that served as the basis to develop the digital model.

3D Digital Phantom Development

The phantom development framework was based on a hybrid model combining the models proposed by S. Gomez et al and Wang et al (S. Gomez et al, 2016; G. Wang et al, 2018). Modifications on their models were implemented to address the bone microarchitectural differences that can be controlled by a set of parameters. The model development framework consists of three steps as shown in Figure 9 below. First, seed-points within a volume of interest are distributed based on a specific distribution that matches the morphology of real bone structure at the site as trabecular bone structures vary at different sites (e.g. trabeculae in vertebral bone is more uniformly distributed and in femoral shaft is more dense around the cortical but hollow in the middle). A fully connected network is then built by connecting each seed-point using Voronoi Tessellation. The number of points in the network determines the density of the cells and is set according to the final trabecular spacing required. The second step is edge pruning and addition of plate-like structures to mimic real-bone looking morphology. Edges can be dropped to create realistic open cell structures following a customizable probability function. Similarly, faces formed by the cells can be randomly added to create plate-like structures as seen in vertebral bone structure. At the end of this step, the basic structure of the bone phantom is developed. Finally, morphological processing steps, including convolution, thresholding and smoothing, to implement

the interconnected structure with controllable trabecular thickness and achieve the specific bone volume fraction required. The model development is written in MATLAB (MATLAB, R2018b).

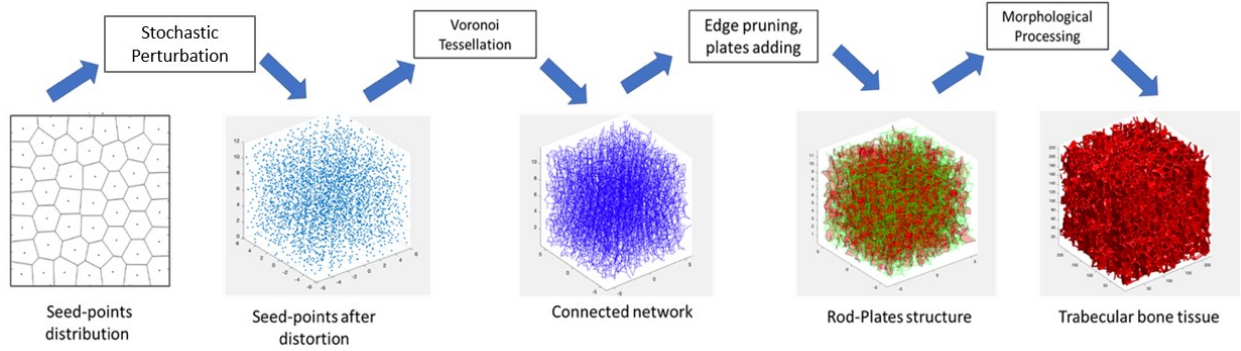


Figure 9. Process of generating trabecular bone-like structure

All the parameters discussed in the following sections can be modified and controlled by the user.

Characterization of the Structure Network

The structure of the trabecular bone network to be simulated is defined according to the following steps. The first step involves setting a volume of interest (VOI) defined by two parameters: the slice height of the volume, and its radius, yielding:

$$volume = slice\ height \times (radius \times 2)^2 \quad (eq. 1)$$

In this study, the slice height is set to 12 mm, with radius of 6 mm, at a resolution of 0.0513 mm/pixel, to have the same dimension as the VOI extracted from the μ CT data. The output volume containing the model is cropped into a matrix of 200 x 200 x 200 voxels.

The second steps sets the target trabecular spacing. The total number of seed-points is determined by the total volume and target spacing:

$$\text{number of points} = (\sqrt[3]{\text{volume}} / \text{spacing})^3 \quad (\text{eq. 2})$$

A variable named z_xy_ratio is set to determine the number of layers in z direction. For a given total number of points, the number of layers in the z direction determines how many seed-points are there on each layer, and the slice height between each layer.

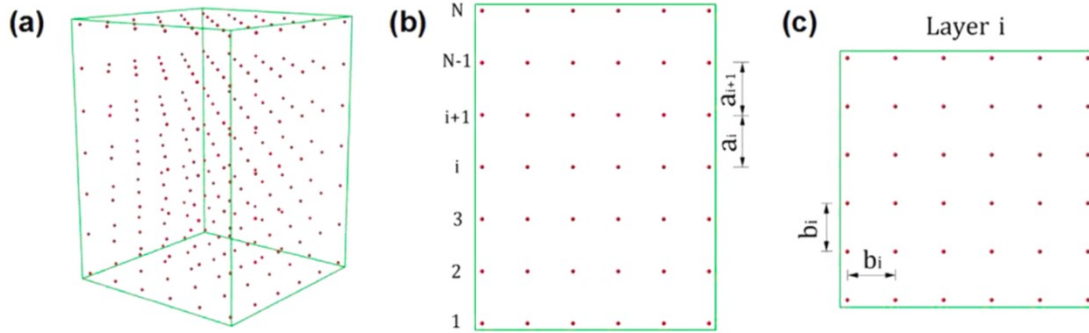


Figure 10 (G. Wang, et al., 2018). Illustration of an example seed-point distribution.

Figure 10 shows a sample regular lattice formed by seed-points within a volume. In (b), there are N layers in the z direction, and the slice height between layer i and layer $i+1$ is labelled as a_i . Layer i contains a total of n points given by

$$n = \text{total number of seed - points} / N \quad (\text{eq. 3})$$

where n is the number of seed-points on each layer. Here, since this sample lattice is regular, the distance between points in the z direction, a , and the distance between points in xy -plane, b , are the same, defined as the target spacing.

On each layer, the sample points are distributed with uniform density as given by a Centroidal Voronoi Tessellation (CVT), as shown in Figure 11. A Voronoi diagram is a way to partition a plane into regions based on the seed-points that the distance to the seed-point of the region from any of the point within that region is closer to the seed than to any, and the regions are called the cells of the Voronoi diagram (G. Voronoy, 1908).

Centroidal Voronoi Tessellation is a special form of Voronoi diagram in which the seed-point of each Voronoi cell is also the centroid of the cell, providing the optimal partitioning of the plane (Q. Du, et al., 1999). The distribution of seed-points provided by CVT yields centroids in uniformly distributed polygons that are used as initial seed-points in our algorithm. At this step, the distribution of seed-points is the same at each layer.

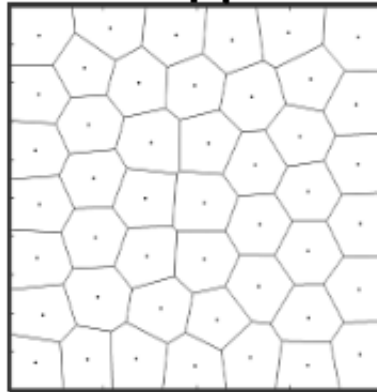


Figure 11. Illustration of Centroidal Voronoi Tessellation



Figure 12 (L. Mosekilde, et al., 1999). A vertebral bone from a young individual

Figure 12 shows the internal bone structure of a vertebral bone from a young healthy individual, and from the shape of the vertebra a flow of trabeculae formation can be seen. In order to control the flow of trabeculae network formation, a gradient along the layers in the z direction is added. In this study, the flow of the structure is according to the following rules (refer back to the notation from Figure 10): for layer index i larger than $N/2$, the seed-points (x,y) location in that layer will shrink towards the center of the volume by a factor of 0.03; for layer index i smaller than $N/2$, the seed-points (x,y) location in that layer will expand outwards by a factor of 0.03. The resulting structure is symmetric to the center plane, xy . Figure 13 shows an illustration of the flow as described.

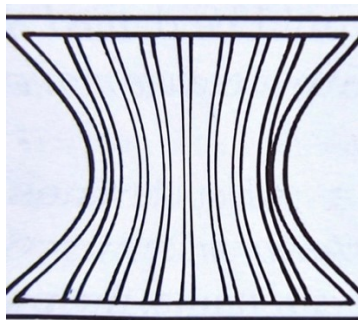


Figure 13. Illustration of the flow along z-direction in this study

Then, a random perturbation in z-direction is added, such that on each layer, the points won't be at the exact same z position. On each layer, the xy-plane is evenly divided into 36 sections, and, at each section, the same random perturbation is added.

Additional randomness is added to the (x,y) location of each seed-point. Figure 14(a) shows a regular lattice and the spheres shown in (b) defines the radius that control the target randomness, with (c) shows the results after disturbance. For a seed-point with location (x,y), the updated coordinates will be:

$$x' = x + R * rand * \sin(\pi * rand) * \cos(2\pi * rand) \quad (\text{eq. 4})$$

$$y' = y + R * rand * \sin(\pi * rand) * \cos(2\pi * rand) \quad (\text{eq. 5})$$

where *rand* is a uniformly distributed random function in the interval of [0, 1].

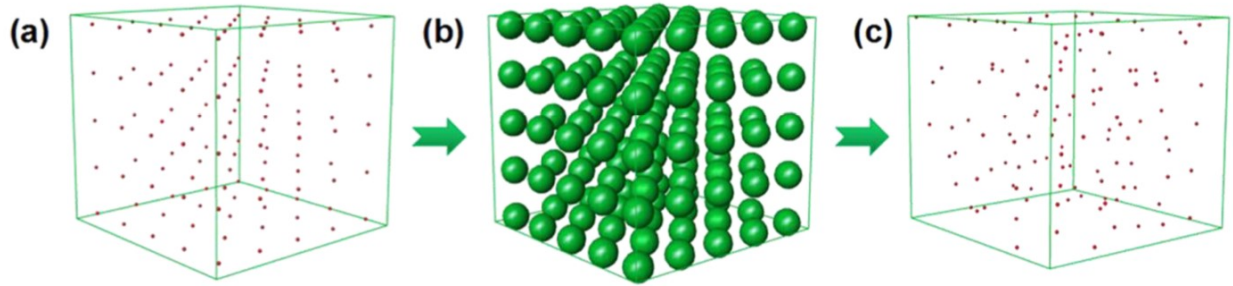


Figure 14 (G. Wang, et al., 2018). A regular lattice is shown in (a), and the green spheres in (b) shows the randomness spheres with radius of $randR$. (c) shows the points after distortion resulting an irregular lattice.

Once the seed-points are distributed as expected, Voronoi Tessellation is used to generate the connected network of the cell frame based on the seed-points. Due to the Voronoi Tessellation

formation theory, the network at the edge will be set to infinity. In order to maintain the network fully connected, only the edges bounded within the VOI are stored.

In the phantom generating framework, the distribution of seed-points can be controlled to characterize the local structure of different sites. For instance, vertebral trabecular bone is denser near the cortical periphery and more porous towards the center of the vertebra. The amount of plate-like structure can be set based on literature to account for bone health level. Examples of variations in bone structure simulated in this work in comparison to their real bone counterparts are shown in Figure 15. Figure 15 illustrates the ability of the phantom model developed in this study to generate a wide range of bone structures with characteristics controlled by user-set parameters.

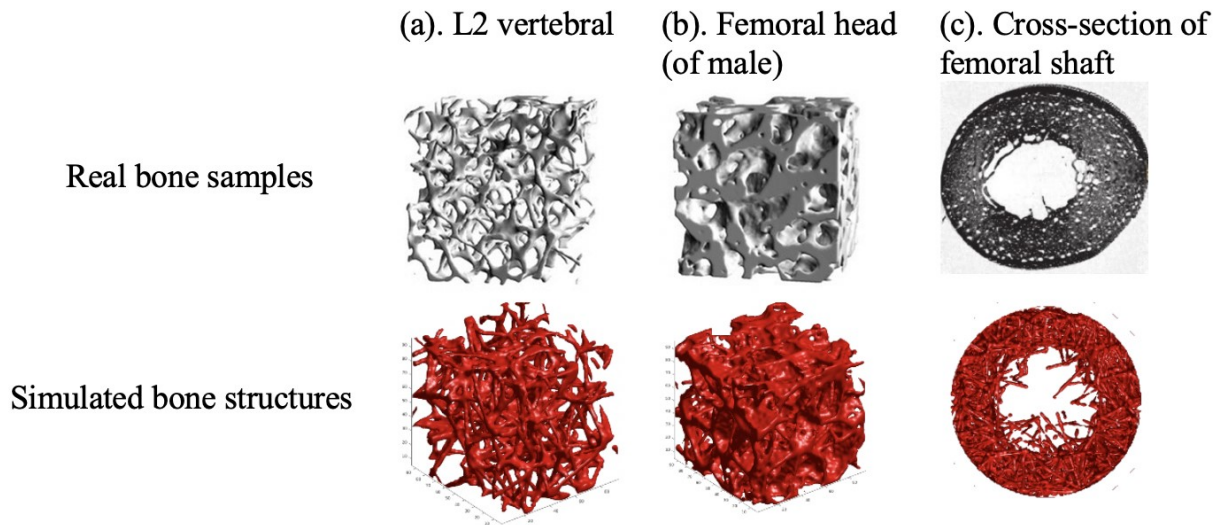


Figure 15. Simulated bone structures (bottom row) with different generating parameters to model the real bone microarchitectures in the top row. Columns (a) and (b) illustrate a variation in plate-like structures, as literature shows there are more plate-like structure in men compared to women at, e.g., the femoral neck (F. Eckstein, et al., 2007); and column (c) shows a non-uniform distribution of cells.

Morphological Processing

Once the fully connected network is built from seed-points, edge pruning and plates addition are applied to the raw structure to generate a more realistic morphology and anatomy compared to real bone.

Figure 16 shows a sample network built on seed-points, and Figure 17 shows a sample Voronoi cell formed by the network. In order to maintain certain morphological characteristics, the position, orientation of each edge needs to be computed by computing the angle between the edge and the z-axis. It can be informed by Figure 12 that most of the trabeculae are lined along the z-axis. To achieve this morphological characteristic, the edges that are more vertical--the angle between the edge and the z-axis is closer to 0, the less likely the edge will be pruned, which is done by setting a probability function. As shown in Figure 17, starting from one vertex (red dot), there may be multiple edges linked to the point; however, there are usually 3-4 edges only linked to one point in real bone setting (F. Zhao, 2018). In this study, the following steps are set to achieve the basic structure: first, the number of edges connected to current point is counted; if the number of edges is less than 4, no pruning is needed, but if the number of edges is either 5 or 6, one randomly selected edge will be dropped, and if the number of edges is larger than 7, then either one or two randomly selected edges will be pruned.

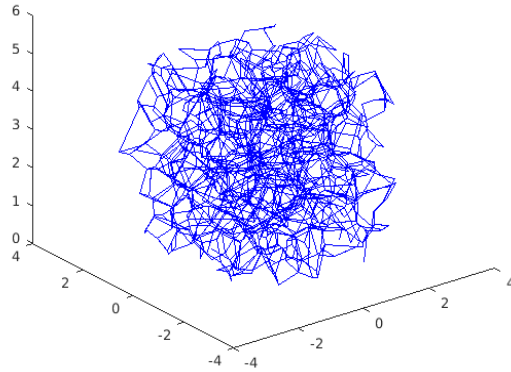


Figure 16. A fully connected network before edge pruning

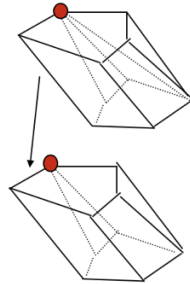


Figure 17. One of the Voronoi cell formed by the network

A similar concept is applied to prune the faces. For each Voronoi cell, there are many faces that together compose the complete volume. For each face, there is a vector orthogonal to it, which is denoted as the face angle. According to Zhao et al (F. Zhao, et al., 2018), based on the observation on vertebral trabecular bone, the distribution of plate orientation shows a small peak at 90° , at colatitude projection (using spherical coordinates from Figure 18) while it is more uniformly distributed elsewhere. The azimuth projection of the plate orientation distribution has two small peaks at the two angles that are perpendicular (e.g., 45° and 135°) depending on the respective 0° . In this study, plates with orientation that are closer to normal to the z-axis (the

colatitude projection is closer to the z-axis), are more likely to remain; plates with orientation on azimuth projection with 45° and 135° are the ones to be kept. Additionally, referring back to figure 12, plates tend to be connected forming long plates, instead of little pieces scattered throughout the whole volume. Thus, when one face is filled, the probability of the faces at its top and bottom will also increase to create long plates, if the top or bottom one has the orientations of both on azimuth projection and on colatitude projection within certain threshold (to create a long-plate along the z-direction).

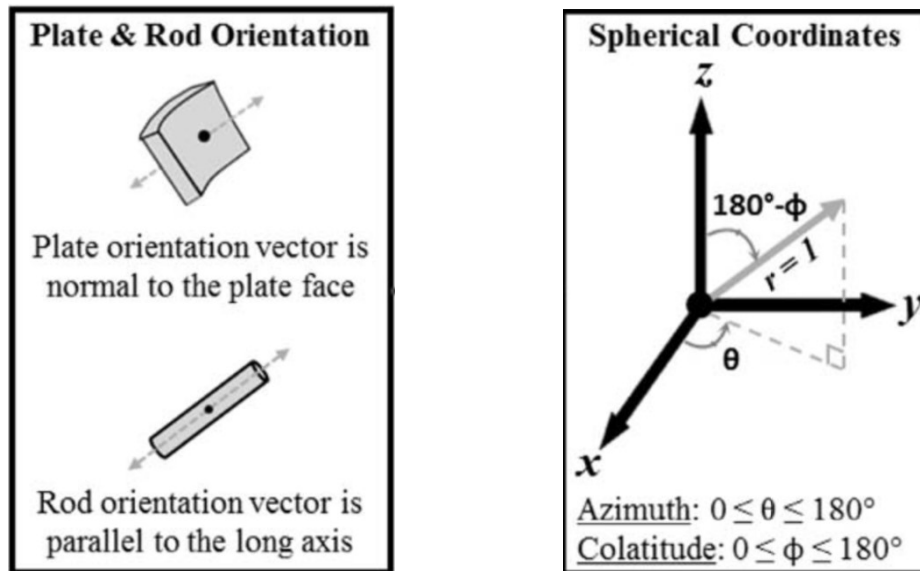


Figure 18 (F. Zhao, et al., 2018). Illustration of the definition of plate and rod orientation.

After the basic structure of the volume is formed with edge pruning and plate addition, we use morphological processing to make the framework achieve certain thickness. With the information of edges and faces referring to rods and plates, a volumetric matrix can be created to generate the 3D structure. In order to be more realistic, for each edge, a weight value is assigned to each position along the length of the edge identified by the network. The distribution of weights is designed to assign larger weights to the end sections, compared to the middle section of the line, since a rod usually has a shape that is thinner in the middle and thicker at the two ends. After

implementing the edge weighting function, convolution and dilation are applied to the structure, to create the thickness of each edge and face. The last step of the phantom generation is to threshold the structure to obtain the desired target bone volume fraction by only keeping the voxels that are over the threshold percentile specified by the bone volume fraction. Figure 19 shows an overall process summary to generate a simulated trabecular bone structure.

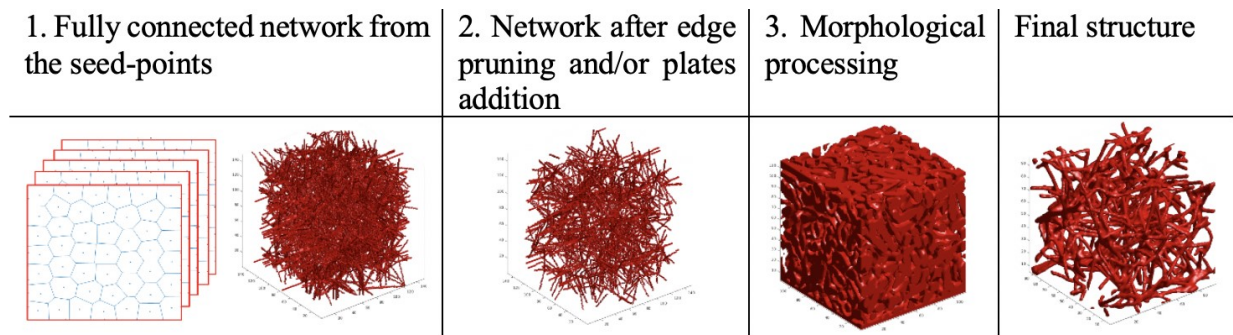


Figure 19. Process of obtaining a simulated trabecular bone structure.

Due to the generating framework, the output structure is very uniform throughout the value with similar trabecular spacing and thickness, while real bones usually show a larger variance. To achieve a realistic variance in the structure, an optional step is added to increase the variation of the two microarchitecture features. Figure 20 shows a Gaussian distributed variation factor matrix that can be convoluted with the original structure to increase variation, where the interpolation is necessary to introduce the transition of variation more smoothly. This step can be executed before the thresholding operation. A random, Gaussian distributed, variation factor is convoluted with the original volume matrix before thresholding. As a result, even with a global threshold value, it is still able to generate a matrix with higher variation.

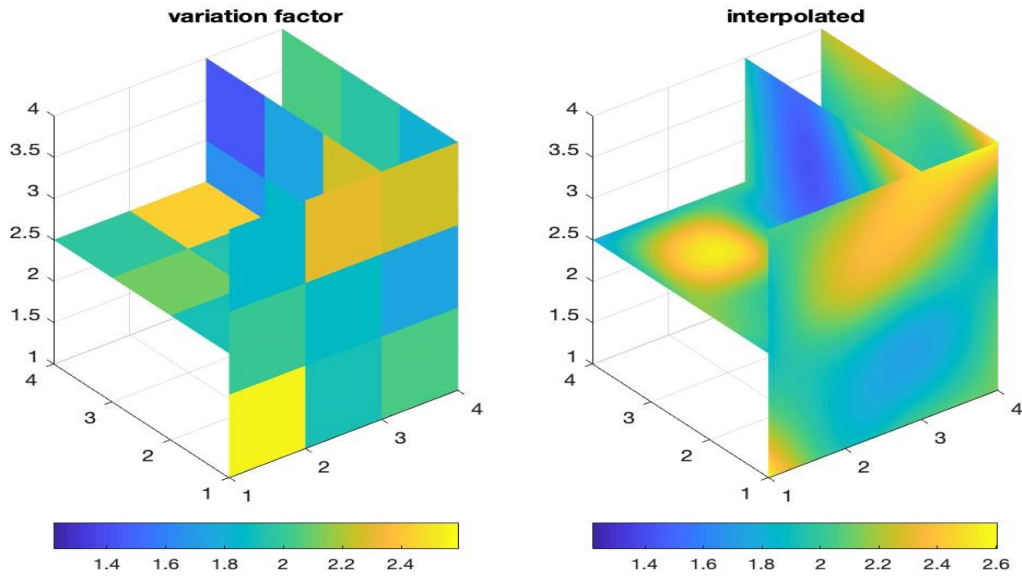


Figure 20. Example of a Gaussian distributed variation factor matrix.

Model Validation

Model validation is an essential part of the study to verify whether the study design is correct. In this study, the model is validated by comparing the microarchitecture measurements and finite element analysis results of the designed model and real bone samples. Statistical analysis is also used to establish correlation between parameters.

Microarchitecture Analysis

A list of commonly used microarchitecture metrics is provided in Table 2. The volume of interest for the analysis was set to 200 x 200 x 200 pixels (isotropic) with pixel size of 0.0513 mm/pixel. The microarchitecture analysis was done with ImageJ, BoneJ plugin (Image J, open source).

Feature	Definition	Unit
Bone Volume Fraction (BVF)	Volume of mineralized bone per unit volume of the sample.	None (ratio)
Connectivity Density (Conn. D.)	Number of trabeculae per unit volume.	(mm ⁻³)
Degree of Anisotropy (D. A.)	A measurement of how highly the trabeculae are oriented in the volume.	None 1 = isotropic ∞ = anisotropy
Trabecular Thickness (Tb. Th.)	The mean thickness of all trabeculae within the bone volume.	mm
Standard Deviation of Tb. Th. (Tb. Th. std)	The standard deviation of the thickness of all the trabeculae within the bone volume.	None
Trabecular Spacing (Tb. Sp.)	The mean spacing between conjunct trabeculae.	mm
Standard Deviation of Tb. Sp. (Tb. Sp. std)	The standard deviation of the mean spacing between conjunct trabeculae.	None

Table 2. List of microarchitecture measurements.

Bone Volume Fraction (BVF):

Bone volume fraction is calculated as the number of foreground (bone) pixels divided by the total number of voxels in the image (BoneJ, ImageJ).

$$BVF = \text{bone volume} / \text{total volume} \quad (\text{eq. 6})$$

Connectivity Density (Conn. D.) (G. Odgaard, 1993):

Trabecular bone is a network with connected structures. The Euler characteristic of the structure can be used to calculate its connectivity. The connectivity density is defined as the overall connectivity estimate divided by the volume. For each voxel that is bone, the Euler characteristic (δ_χ) is computed and the overall Euler characteristic is calculated as:

$$\chi = \sum \delta_\chi \quad (\text{eq. 7})$$

The contribution of the bone sample to the overall Euler characteristic ($\Delta\chi$) is measured by checking the intersections of voxels and the volume edges. Then the connectivity is defined as:

$$\beta = 1 - \Delta\chi \quad (\text{eq. 8})$$

Finally, the connectivity density is given by:

$$\text{Conn. D.} = \beta / \text{volume} \quad (\text{eq. 9})$$

Degree of Anisotropy (D. A.):

The mean intercept length (MIL) method (H. Mann, 1984) is used to compute the anisotropy in the BoneJ plugin. From a random point within the volume, a large number of vectors with the same length can be drawn. For each of the vectors, an intercept is counted when it hits a boundary between the foreground and the background. MIL can then be calculated by dividing the vector length by the number of boundary hits. A collection of points is built up, and each point represents a value of the vector times its MIL. The point cloud is then fitted with an ellipsoid. The ellipsoid eigenvalues can then be calculated obtaining the construction of the structure anisotropy tensor, since the eigenvectors are the axis of the ellipsoid. The degree of anisotropy is then defined as:

$$DA = \text{long axis eigenvalue} / \text{short axis eigenvalue} \quad (\text{eq. 10})$$

Trabecular Spacing (Tb. Sp.):

The trabecular spacing is defined as the diameter of the greatest sphere that can be fitted within the non-bone region at a point (background). The spacing measurement is run on all spheres filled in background. A map of pixels is generated, with each pixel has the value of greatest sphere can be generated from that pixel, as shown in Figure 21 (right). Then, the mean value and standard deviation are computed directly from pixel values.

Trabecular Thickness (Tb. Th.):

The trabecular thickness is defined as the diameter of the greatest sphere that can be fitted within the bone structure at a point (foreground). The thickness measurement is run on all the spheres filled in foreground. A map of pixels is generated, with each pixel has the value of greatest sphere can be generated from that pixel, as shown in Figure 21 (left). Then the mean value and standard deviation are computed directly from pixel values.

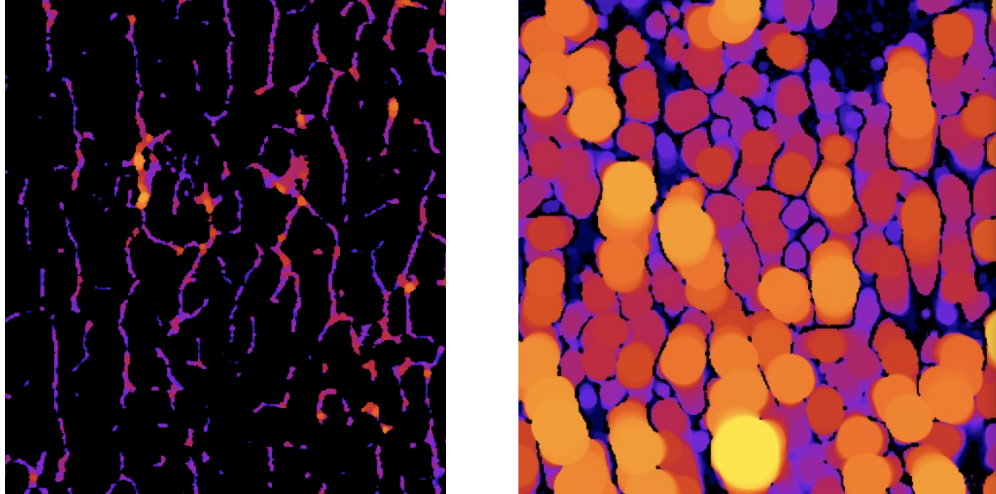


Figure 21. Thickness map of (left) trabecular thickness and (right) trabecular spacing.

The BoneJ plugin used for the measurements described above requires a binary image input with values in grayscale (0/255), and the analysis is run assuming trabeculae are the foreground pixels, with value of 255. Post-processing of the image data is essential to obtain consistent measurements. The image processing pipeline before microarchitecture measurements is as following (names of process operations are based on ImageJ), with the key steps shown in Figure 22:

Step 1: Import image sequence into ImageJ.

Step 2: Upscale the volume in a scale factor of 2 for x, y, z directions using bilinear interpolation.

Step 3: Apply a 3D Laplace kernel to the volume to enhance the contrast between bone and background.

Step 4: Crop the volume into $[2:n-1, 2:n-1, 2:n-1]$ to remove edge effects from convolution operations.

Step 5: Apply the ROF denoising algorithm (L. Rudin, et al., 1992) with noise sigma of 200.

Step 6: Binarize the volume using the Isodata algorithm (T. Ridler, et al., 1978), with global thresholding.

Step 7: Purify the image to only remain the largest foreground and background particles and remove the rest in order to obtain one fully connected structure and remove all floating parts.

Step 8: Run microarchitecture measurements with the BoneJ plugin (Double M, et al., 2010).

The same processing pipeline is applied to both human data and developed models with same VOI size.

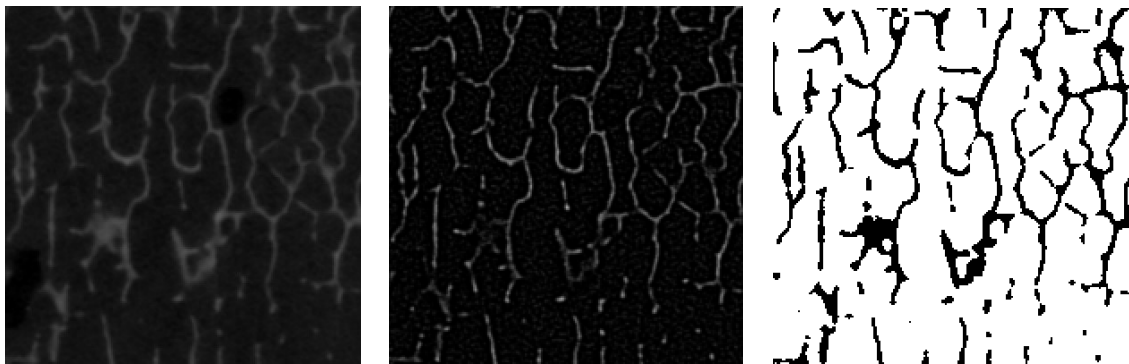


Figure 22. Left shows an original image; middle shows the image after Laplace kernel; and right is the image after binarization that will read in BoneJ.

Finite Element Analysis

Finite element analysis is used to measure the stiffness of the structure. In this study, stiffness refers to the compressive stiffness along the principle loading direction as shown in Figure 23, defined as

$$\text{stiffness} = \text{load} / \text{displacement} \quad \text{unit: [N/mm]} \quad (\text{eq. 11})$$

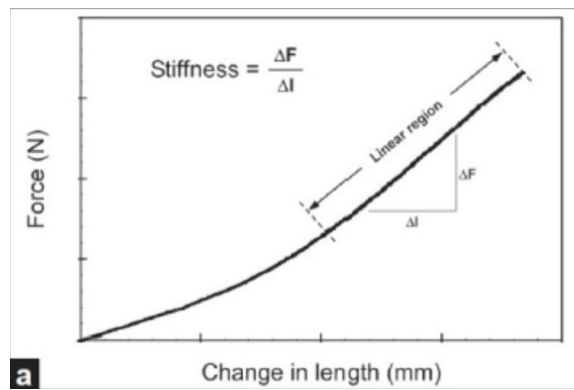


Figure 23. Illustration of the definition of stiffness

The software used to complete the finite element analysis is Abaqus (ABAQUS Inc.), and the meshing process of the volume structure is encoded in MATLAB.

In order to apply a uniform load onto the structure, two plates with thickness of 5 pixels in the z direction are added to the top and bottom of the structure. The bone structure with the added plates is then converted into a mesh in tetrahedron elements. Figure 24 shows a real bone structure with added covers in mesh.

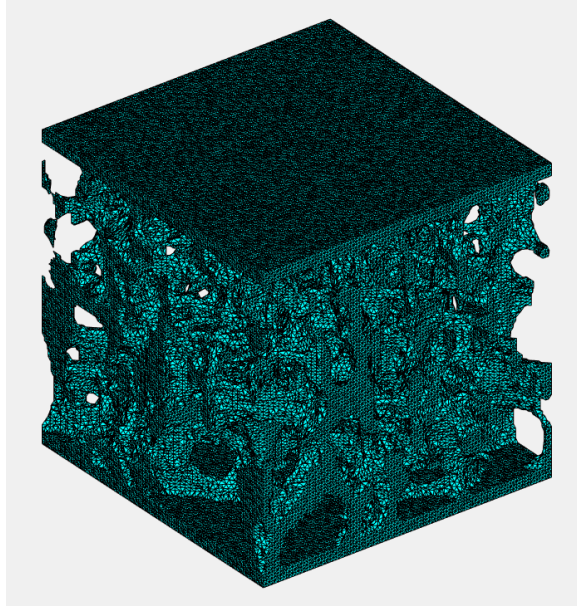


Figure 24. Bone structure extracted from one of the real bone specimens, converted into mesh with tetrahedron elements.

The meshed structure is then loaded into Abaqus to complete the finite element analysis. The structure is assigned with elastic property: elastic modulus of 13.4 GPa, and Poisson's ratio of 0.3. The bottom of the structure is fixed, with a uniformly distributed load applied onto the top plate, to achieve a 3% displacement along the z-axis. The reaction force at the bottom plate is stored as the load, together with the 3% displacement in units of millimeters, to compute the stiffness of the structure. Figure 25 shows an output visualization from Abaqus.

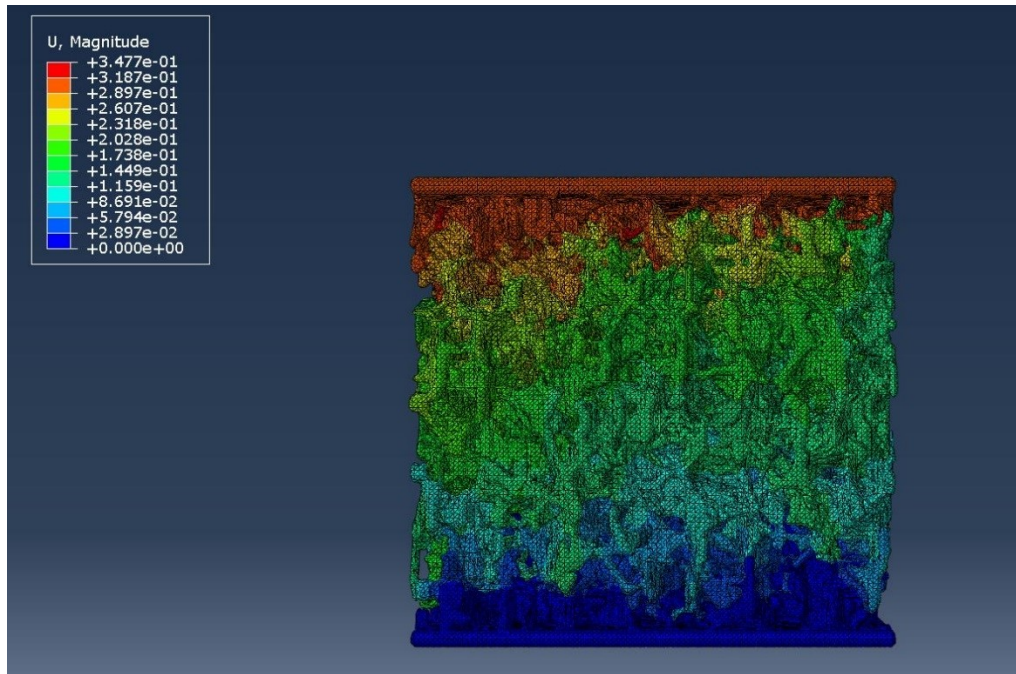


Figure 25. A visualization of the output of Abaqus, U is the displacement in unit of millimeter.

Statistical Analysis

Statistical analysis was used to develop a more quantitative measurement of the parameters and assist in the discovery of potential patterns or correlations between the parameters. The statistical analysis was done on Rstudio (Rstudio, Inc.) and MATLAB.

The histogram of each microarchitecture feature was computed for both the human dataset and the library of developed digital phantoms. With the histogram, the distribution function was also produced.

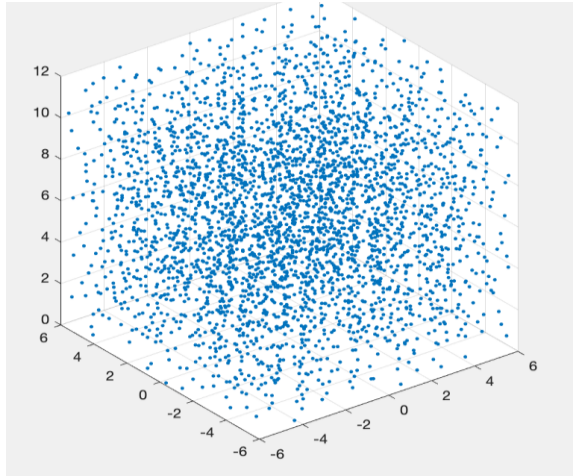
Correlation of the microarchitecture features was investigated to underlying morphological and physical representation of each parameter. Also, correlation of the input variables of the

phantom generating pipeline to the measured microarchitecture features of the output was used to calibrate the mathematical expression used within the development codes. It is essential to include this correlation, since not all of the microarchitecture features are directly controlled by single input variables but may be determined by a combination of them.

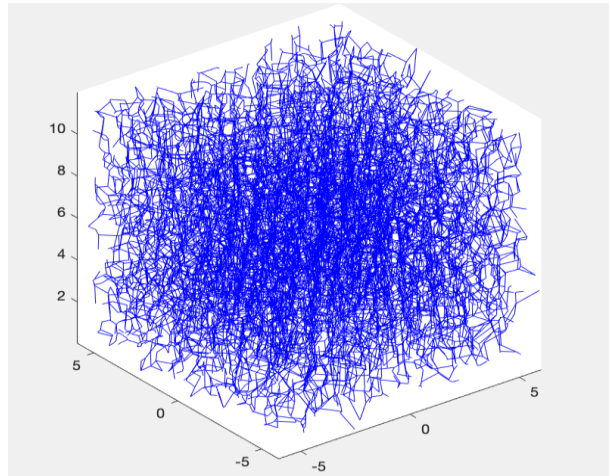
Chapter III

Results

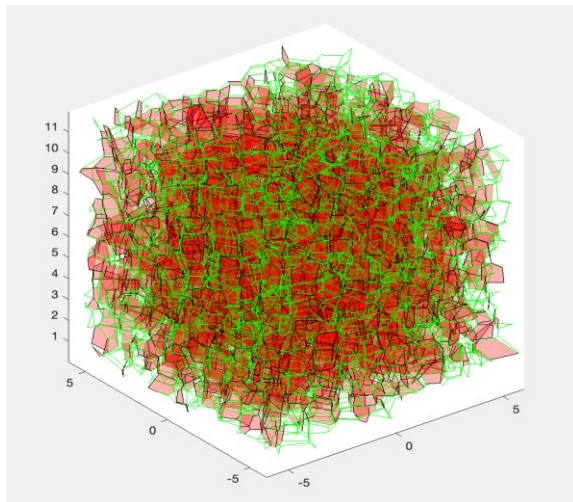
Graphical 2D and 3D Visualization



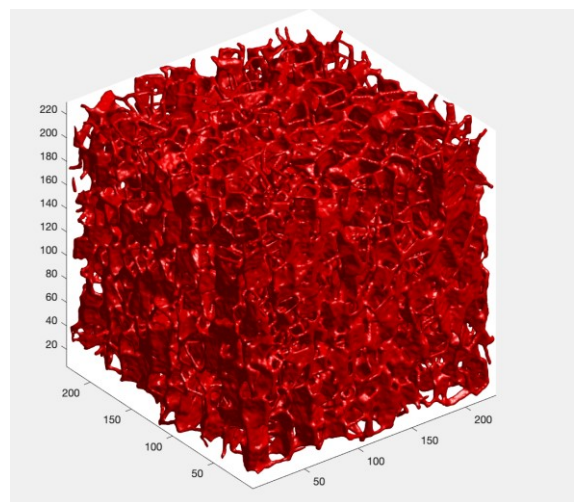
(a)



(b)



(c)



(d)

Figure 26. (a) Seed-points were distributed as described in Chapter II. (b) A fully connected network was formed by Voronoi Tessellation from the seed-points in (a). (c) The network of rods after edge pruning is shown in green, and the selectively filled faces representing the plates are in red. (d) Complete structure after morphological processing.

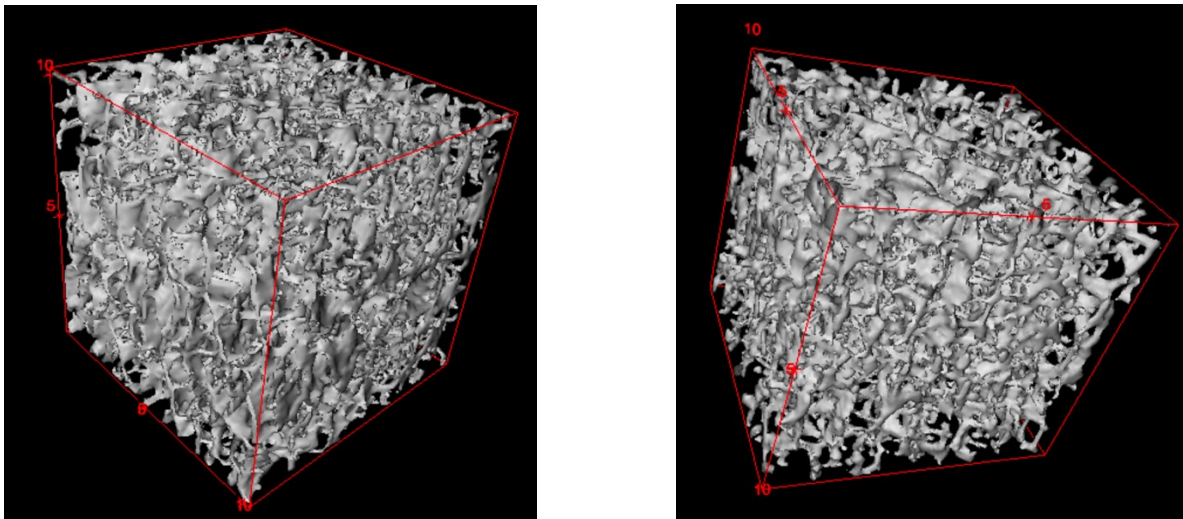
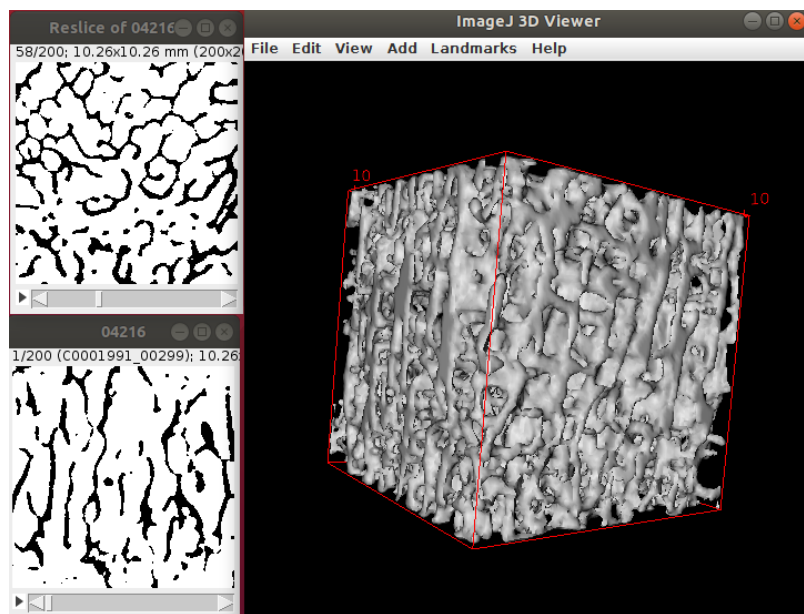
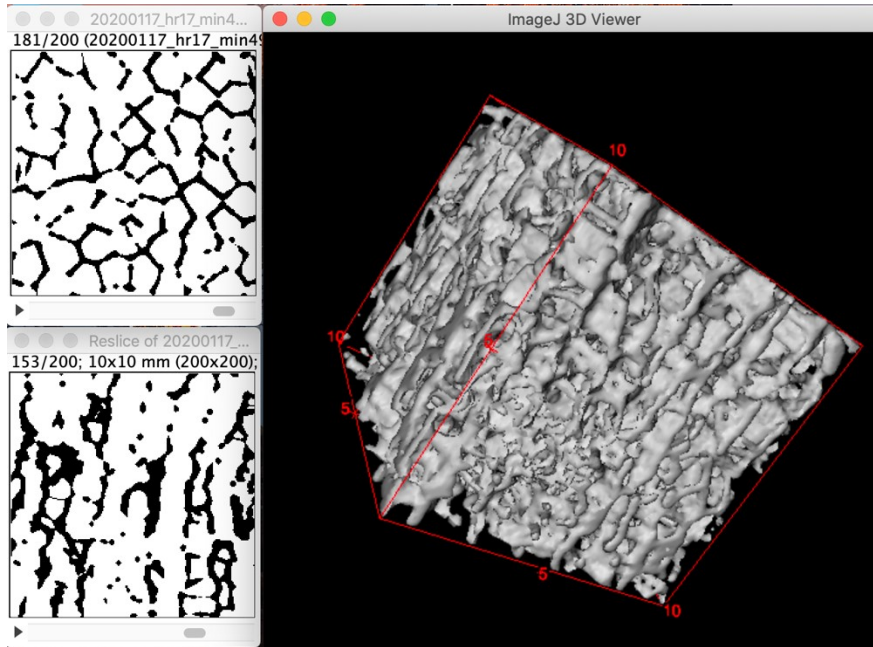


Figure 27. Left shows a 3D visualization of a VOI extracted from a human bone specimen, and right shows a 3D visualization of a model generated by the designed framework, with similar trabecular microarchitecture features as the left bone volume.



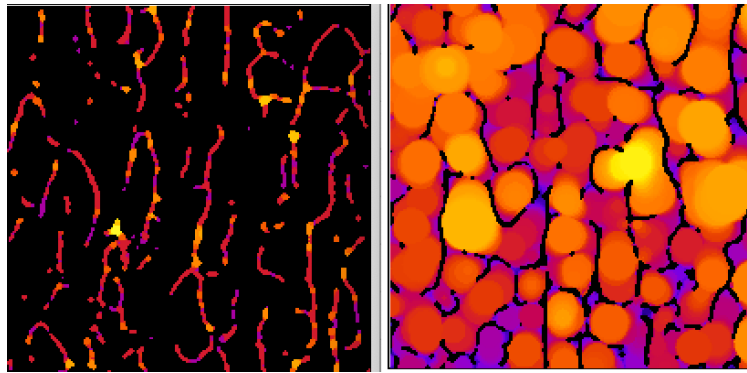
(a)



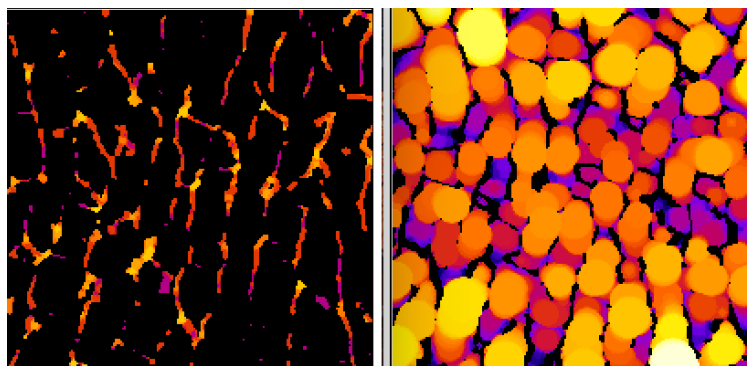
(b)

Figure 28. (a) A real bone structure and (b) a simulated bone phantom with bone volume fraction of about 0.2 ($BV/TV = 20\%$), with 2D visualization of selected slice from both xy-plane and xz-plane view.

Comparing Figure 27 and Figure 28, real bone structure is more diverse and have more obvious variation in the structure throughout the volume whereas the simulated model is more uniform in trabecular spacing and trabecular thickness. Additionally, the real bone structure has a more smooth curvature of each trabecula, while the simulated model is more rigid at the turning points. Although variation was added before thresholding, the distribution of the seed-points determined the general structure, such that big variations in structure can hardly be seen without adding more variation during the points distributing step. Figure 29 shows the real bone structure and simulated digital phantom in distance map view.



(a)



(b)

Figure 29. Distance map of a selected slice of a real bone (a) and a corresponding digital phantom (b) generated based on the microarchitecture features of the real bone.

Microarchitecture Features

As mentioned in Chapter II, several commonly used microarchitecture features are measured using ImageJ, BoneJ plugin, namely: bone volume fraction (BVF), connectivity density (Conn.D), degree of anisotropy (DA), trabecular thickness (Tb. Th), trabecular spacing (Tb. Sp).

Since the microarchitecture features are not the direct input of the phantom generating program, investigation on the correlation of input variables to the microarchitecture measurements is needed. There are tens of modifiable variables in the program, however, most of them are set to their default value for now, and only a few that may lead to direct changes in the structure were changed for different target structures: bone volume fraction, trabecular spacing, randR, and z_xy_ratio. In order to evaluate the effect of each variable, 375 models were generated with the following parameters: bone volume fraction of 0.1, 0.2, and 0.3; trabecular spacing of 0.7, 0.9, 1.1, 1.3, 1.5; randR, to control the randomness level, of 0, 0.2, 0.4, 0.6, 0.8; z_xy_ratio, to control the shape of the faces formed by the network, of 0.6, 0.8, 1, 1.2, 1.4.

Models	bvf	tbsp	randR	zxyratio	Bone Volume (mm ³)	Total Volume(mm ³)	Volume Ratio	Conn. Density (mm ³)	Degree of Anisotropy	Tb.Th Mean (mm)	Tb.Th STD	Tb.Sp Mean	Tb.Sp STD
bvf0.1_tbsp0.7_randRO_zxyratio0.6	0.10	0.70	0.00	0.60	56.84	505.01	0.11	4.12	0.31	0.16	0.05	0.65	0.15
bvf0.1_tbsp0.7_randRO_zxyratio0.8	0.10	0.70	0.00	0.80	55.96	505.01	0.11	4.70	0.34	0.15	0.05	0.66	0.15
bvf0.1_tbsp0.7_randRO_zxyratio1	0.10	0.70	0.00	1.00	55.65	505.01	0.11	5.94	0.34	0.15	0.05	0.68	0.15
bvf0.1_tbsp0.7_randRO_zxyratio1.2	0.10	0.70	0.00	1.20	56.89	505.01	0.11	7.87	0.35	0.15	0.05	0.70	0.16
bvf0.1_tbsp0.7_randRO_zxyratio1.4	0.10	0.70	0.00	1.40	56.64	505.01	0.11	7.88	0.34	0.15	0.05	0.77	0.24
bvf0.1_tbsp0.7_randRO.2_zxyratio0.6	0.10	0.70	0.20	0.60	56.27	505.01	0.11	3.99	0.30	0.16	0.06	0.65	0.15
bvf0.1_tbsp0.7_randRO.2_zxyratio0.8	0.10	0.70	0.20	0.80	56.37	505.01	0.11	4.80	0.32	0.15	0.05	0.65	0.15
bvf0.1_tbsp0.7_randRO.2_zxyratio1	0.10	0.70	0.20	1.00	57.74	505.01	0.11	6.29	0.34	0.15	0.05	0.67	0.15
bvf0.1_tbsp0.7_randRO.2_zxyratio1.2	0.10	0.70	0.20	1.20	57.19	505.01	0.11	7.95	0.33	0.15	0.05	0.70	0.17
bvf0.1_tbsp0.7_randRO.2_zxyratio1.4	0.10	0.70	0.20	1.40	55.56	505.01	0.11	7.69	0.32	0.15	0.04	0.75	0.22
bvf0.1_tbsp0.7_randRO.4_zxyratio0.6	0.10	0.70	0.40	0.60	58.26	505.01	0.12	4.19	0.28	0.16	0.06	0.64	0.14
bvf0.1_tbsp0.7_randRO.4_zxyratio0.8	0.10	0.70	0.40	0.80	56.39	505.01	0.11	5.33	0.30	0.15	0.05	0.65	0.14
bvf0.1_tbsp0.7_randRO.4_zxyratio1	0.10	0.70	0.40	1.00	55.55	505.01	0.11	5.75	0.30	0.15	0.05	0.67	0.15
bvf0.1_tbsp0.7_randRO.4_zxyratio1.2	0.10	0.70	0.40	1.20	56.77	505.01	0.11	7.00	0.29	0.15	0.05	0.69	0.16
bvf0.1_tbsp0.7_randRO.4_zxyratio1.4	0.10	0.70	0.40	1.40	55.64	505.01	0.11	7.08	0.30	0.15	0.04	0.73	0.20
bvf0.1_tbsp0.7_randRO.6_zxyratio0.6	0.10	0.70	0.60	0.60	57.56	505.01	0.11	3.86	0.27	0.16	0.06	0.64	0.14
bvf0.1_tbsp0.7_randRO.6_zxyratio0.8	0.10	0.70	0.60	0.80	56.58	505.01	0.11	4.66	0.28	0.16	0.05	0.65	0.14
bvf0.1_tbsp0.7_randRO.6_zxyratio1	0.10	0.70	0.60	1.00	55.94	505.01	0.11	5.92	0.28	0.15	0.05	0.66	0.15
bvf0.1_tbsp0.7_randRO.6_zxyratio1.2	0.10	0.70	0.60	1.20	56.30	505.01	0.11	6.45	0.27	0.15	0.05	0.68	0.16
bvf0.1_tbsp0.7_randRO.6_zxyratio1.4	0.10	0.70	0.60	1.40	56.51	505.01	0.11	6.41	0.26	0.15	0.05	0.70	0.19
bvf0.1_tbsp0.7_randRO.8_zxyratio0.6	0.10	0.70	0.80	0.60	57.08	505.01	0.11	3.80	0.27	0.16	0.06	0.66	0.15
bvf0.1_tbsp0.7_randRO.8_zxyratio0.8	0.10	0.70	0.80	0.80	54.68	505.01	0.11	4.35	0.26	0.16	0.05	0.66	0.14
bvf0.1_tbsp0.7_randRO.8_zxyratio1	0.10	0.70	0.80	1.00	57.10	505.01	0.11	5.47	0.27	0.16	0.05	0.66	0.15
bvf0.1_tbsp0.7_randRO.8_zxyratio1.2	0.10	0.70	0.80	1.20	57.11	505.01	0.11	6.13	0.25	0.15	0.05	0.67	0.16
bvf0.1_tbsp0.7_randRO.8_zxyratio1.4	0.10	0.70	0.80	1.40	56.35	505.01	0.11	5.98	0.25	0.15	0.05	0.69	0.18
bvf0.1_tbsp0.9_randRO_zxyratio0.6	0.10	0.90	0.00	0.60	57.17	505.01	0.11	9.05	0.37	0.14	0.04	0.72	0.18
bvf0.1_tbsp0.9_randRO_zxyratio0.8	0.10	0.90	0.00	0.80	55.62	505.01	0.11	7.15	0.38	0.13	0.04	0.76	0.17
bvf0.1_tbsp0.9_randRO_zxyratio1	0.10	0.90	0.00	1.00	55.87	505.01	0.11	7.18	0.40	0.13	0.04	0.78	0.17
bvf0.1_tbsp0.9_randRO_zxyratio1.2	0.10	0.90	0.00	1.20	55.20	505.01	0.11	5.18	0.40	0.13	0.04	0.85	0.20
bvf0.1_tbsp0.9_randRO_zxyratio1.4	0.10	0.90	0.00	1.40	55.15	505.01	0.11	4.77	0.38	0.14	0.04	0.90	0.21
bvf0.1_tbsp0.9_randRO.2_zxyratio0.6	0.10	0.90	0.20	0.60	56.16	505.01	0.11	8.38	0.36	0.14	0.04	0.72	0.18
bvf0.1_tbsp0.9_randRO.2_zxyratio0.8	0.10	0.90	0.20	0.80	56.43	505.01	0.11	7.24	0.39	0.14	0.04	0.75	0.18
bvf0.1_tbsp0.9_randRO.2_zxyratio1	0.10	0.90	0.20	1.00	54.68	505.01	0.11	6.43	0.38	0.13	0.04	0.78	0.17
bvf0.1_tbsp0.9_randRO.2_zxyratio1.2	0.10	0.90	0.20	1.20	53.71	505.01	0.11	6.01	0.39	0.13	0.04	0.84	0.20
bvf0.1_tbsp0.9_randRO.2_zxyratio1.4	0.10	0.90	0.20	1.40	55.83	505.01	0.11	5.63	0.37	0.14	0.04	0.87	0.22
bvf0.1_tbsp0.9_randRO.4_zxyratio0.6	0.10	0.90	0.40	0.60	56.70	505.01	0.11	8.92	0.35	0.14	0.04	0.73	0.17
bvf0.1_tbsp0.9_randRO.4_zxyratio0.8	0.10	0.90	0.40	0.80	56.63	505.01	0.11	7.75	0.35	0.14	0.04	0.74	0.17

Table 3. Look-up table of the 375 models with input variables and output structures' microarchitecture measurements.

The effect of each input variable on the output measurements was evaluated with Pearson's correlation test. The correlogram was used to visualize the correlation, as shown in Figure 30.

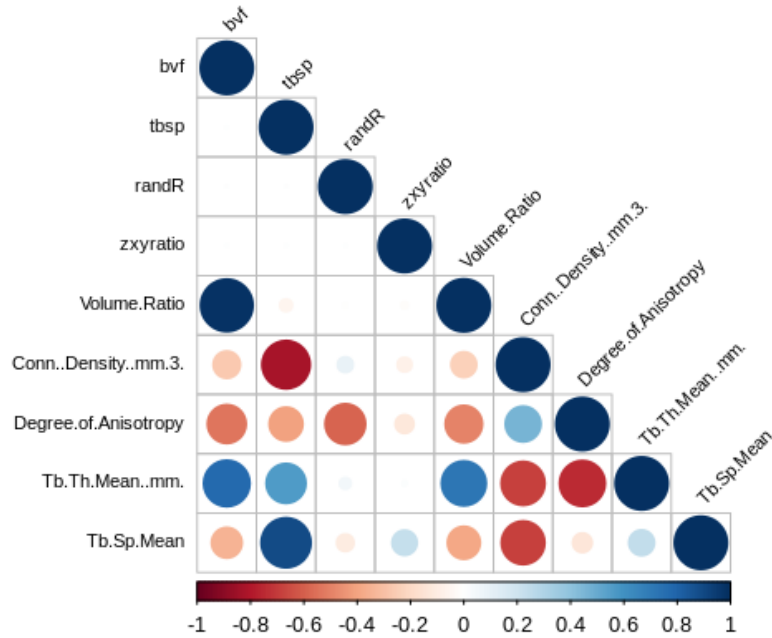


Figure 30. Visualization of the correlation using correlogram. The variables in lower case are input variables, and the variables in upper case are measured values from ImageJ.

According to Figure 30 volume ratio is directly related to input bone fraction. Conn. D is inversely related to input trabecular spacing. Degree of anisotropy is inversely related to input bone volume fraction, trabecular spacing, and randR. The measured trabecular thickness positively correlates with the input bone volume fraction and trabecular spacing. The measured trabecular spacing is directly related to input value, and inversely related to input bone volume fraction.

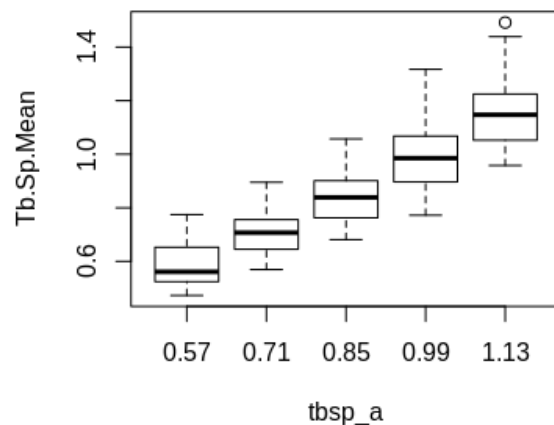
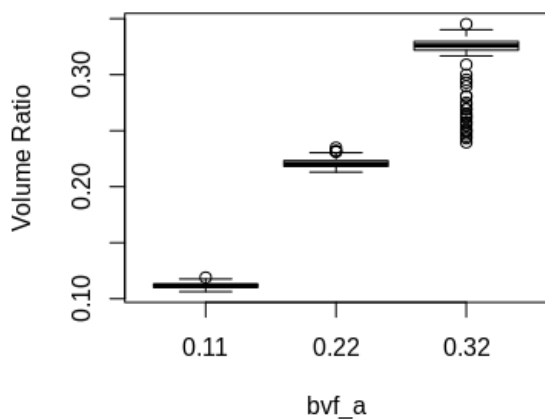


Figure 31. Boxplot of bone volume ratio and trabecular spacing. x-axis represents the input values, and y-axis represents the feature measurement of the output structure. bvf_a and tbsp_a are the calibrated values to achieve linear regression in a factor of 1.

The target value and measured results of bone volume fraction and trabecular spacing both showed a good agreement as expected by design.

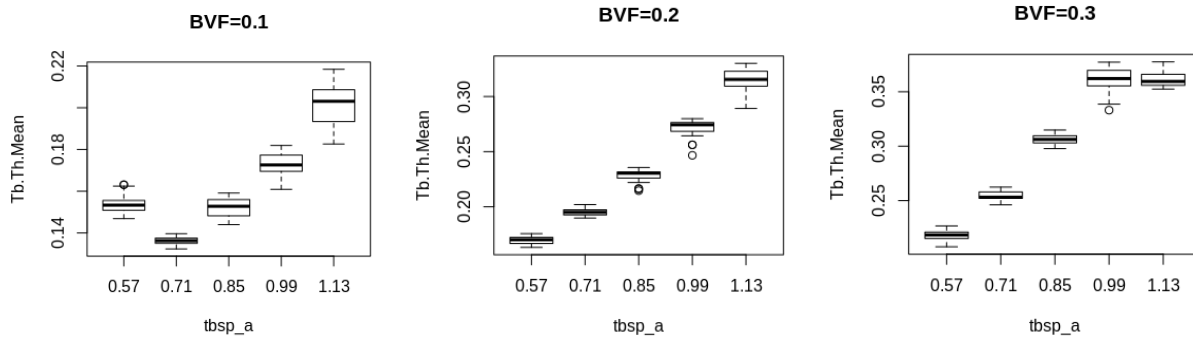


Figure 32. Boxplot of measured trabecular thickness to the input trabecular spacing at certain levels of input bone volume fraction.

Theoretically, with a fixed BVF, trabecular thickness and trabecular spacing should be in positive correlation, as the spacing is larger, the mean thickness of trabeculae has to be larger to reach the same level of bone value fraction. The same results are shown in Figure 31, while there are two exceptions--when both BVF and spacing are small, and when both are larger. However, this two cases are actually not realistic for the bone structure. When the BVF is small, the structure should be more porous and it is hard to have small spacing; vice versa, when the BVF is large, the structure will be denser, and it is hard to have large spacing.

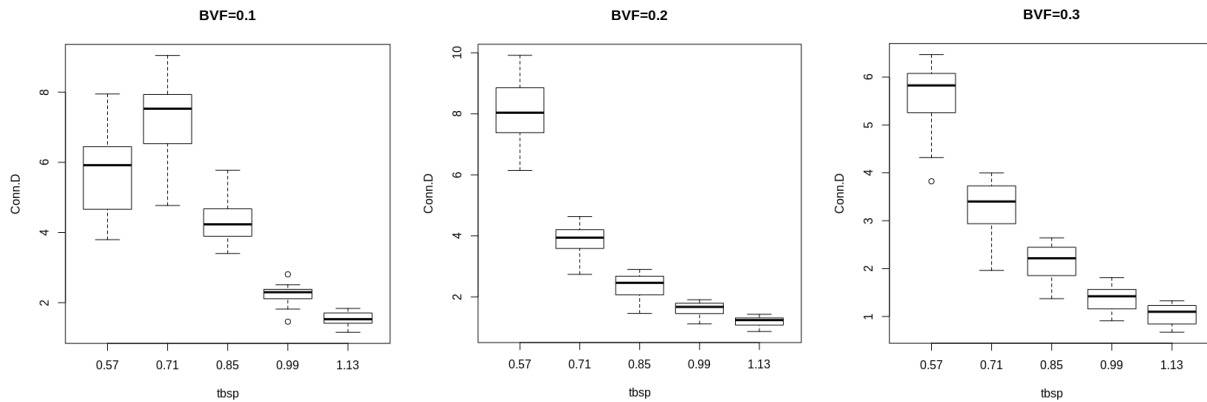


Figure 33. Boxplot of connectivity density to the input trabecular spacing at certain levels of input bone volume fraction.

Connectivity density is the number of trabeculae per volume, so theoretically it should be inversely related to trabecular spacing, since larger spacing between trabeculae leads to a less dense structure with smaller number of trabeculae within each volume. Figure 33 shows the model results showing the expected trends, with exception similar to the one mentioned previously--at low BVF, small trabecular spacing is hard to reach, and so the outlier can be neglected.

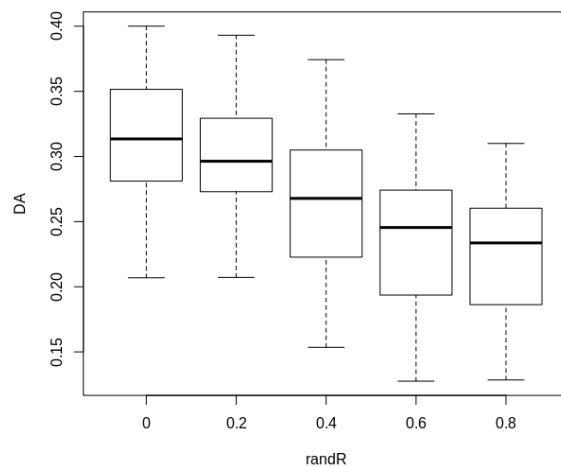


Figure 34. Boxplot of input randR to measured degree of anisotropy.

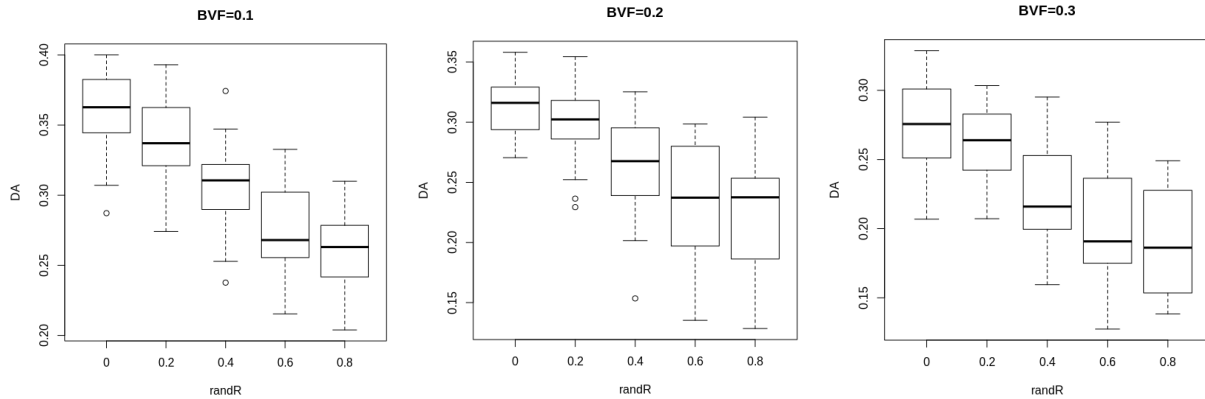


Figure 35. Boxplot of input randR to measured degree of anisotropy at certain levels of input bone volume fraction.

With same level of bone volume fraction, degree of anisotropy is inversely correlated to input randR. Theoretically, randR is the radius of the randomness sphere at the step of seed-points distribution, and so the larger the value of randR, the less oriented the structure is, leading to a smaller DA.

In order to validate the model design algorithm, first a volume of interest was extracted from a real bone sample, then the microarchitecture analysis were applied to the VOI. The measurements were then used as the target values to be reached by the simulated model.

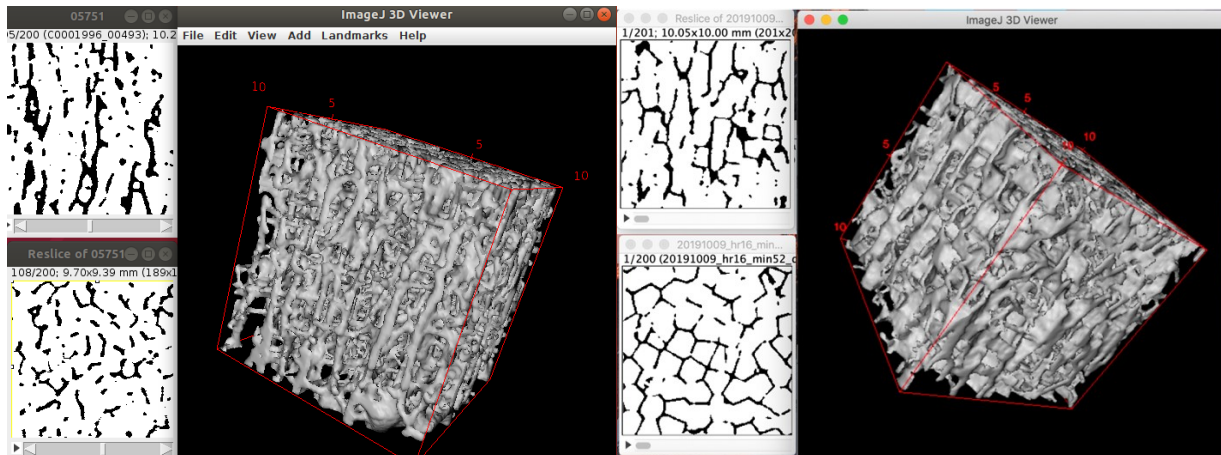


Figure 36. VOI extracted from patient 05751 (left) and corresponding simulated structure (right).

	Volume Ratio	Conn. Density	Tb.Th Mean	Tb.Th STD	DA	Tb.Sp Mean	Tb.Sp STD
real 05751	0.1552	2.4900	0.2326	0.0604	0.3065	0.9445	0.2857
model	0.1653	2.4324	0.1924	0.0430	0.3089	0.9523	0.2106
ERROR	6.51%	-2.32%	-17.30%	-28.76%	0.78%	0.82%	-26.29%

Table 4. Microarchitecture measurements of the structures in Figure 36.

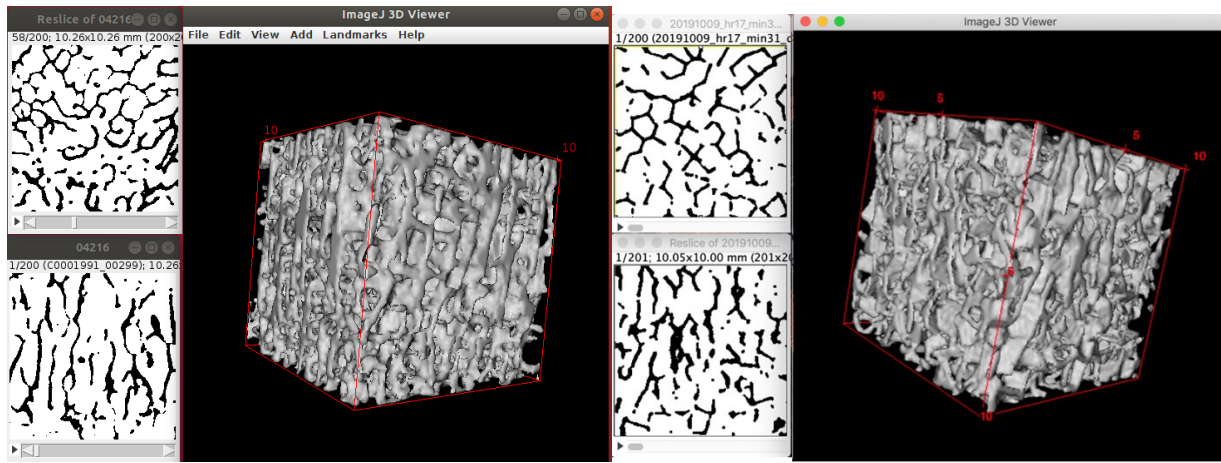


Figure 37. VOI extracted from patient 04216 (left) and corresponding simulated structure (right).

	Volume Ratio	Conn. Density	Tb.Th Mean	Tb.Th STD	DA	Tb.Sp Mean	Tb.Sp STD
real 04216	0.2151	2.6024	0.2557	0.0792	0.2776	0.8165	0.2312
model	0.2205	2.5440	0.2339	0.0435	0.2627	0.8313	0.1961
ERROR	2.51%	-2.24%	-8.50%	-45.05%	-5.37%	1.82%	-15.19%

Table 5. Microarchitecture measurements of the structures in Figure 37.

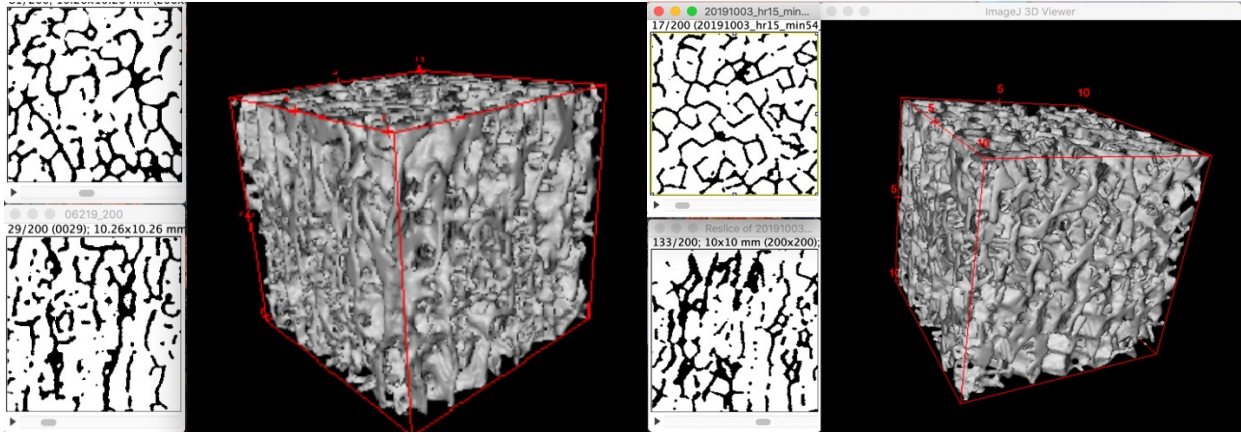


Figure 38. VOI extracted from patient 06219 (left) and corresponding simulated structure (right).

	Volume Ratio	Conn. Density	Tb.Th Mean	Tb.Th STD	DA	Tb.Sp Mean	Tb.Sp STD
real 06219	0.2254	3.0808	0.2642	0.0887	0.2113	0.8367	0.2522
model	0.2205	2.9525	0.2153	0.0418	0.2462	0.7877	0.1980
ERROR	-2.17%	-4.16%	-18.50%	-52.87%	16.55%	-5.86%	-21.49%

Table 6. Microarchitecture measurements of the structures in Figure 38.

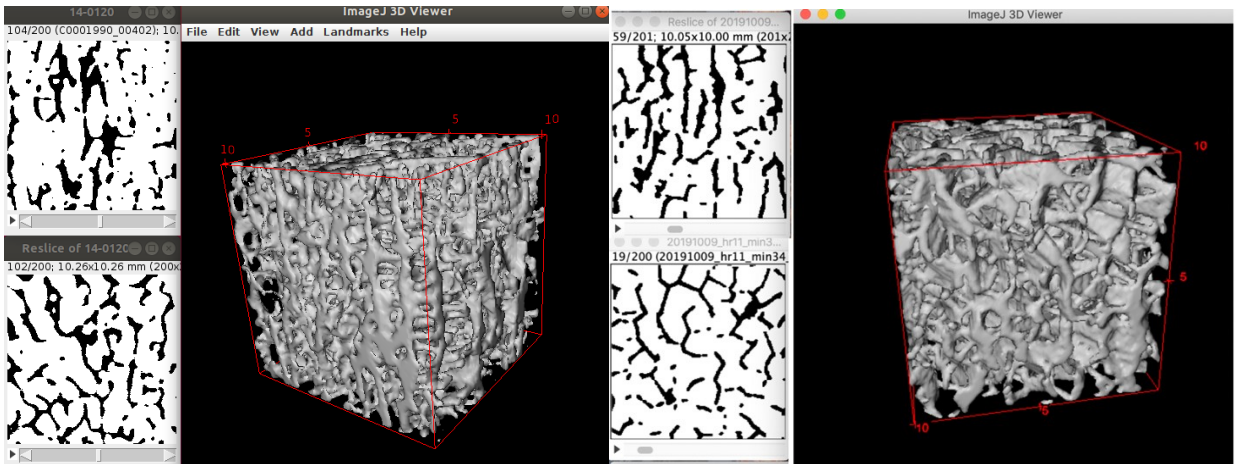


Figure 39. VOI extracted from patient 14-0120 (left) and corresponding simulated structure (right).

	Volume Ratio	Conn. Density	Tb.Th Mean	Tb.Th STD	DA	Tb.Sp Mean	Tb.Sp STD
real 14-0120	0.1940	1.8886	0.3206	0.1298	0.2817	0.9723	0.2679
model	0.2012	1.7433	0.2619	0.0478	0.2449	1.0046	0.2526
ERROR	3.74%	-7.70%	-18.32%	-63.15%	-13.06%	3.32%	-5.72%

Table 7. Microarchitecture measurements of the structures in Figure 39.

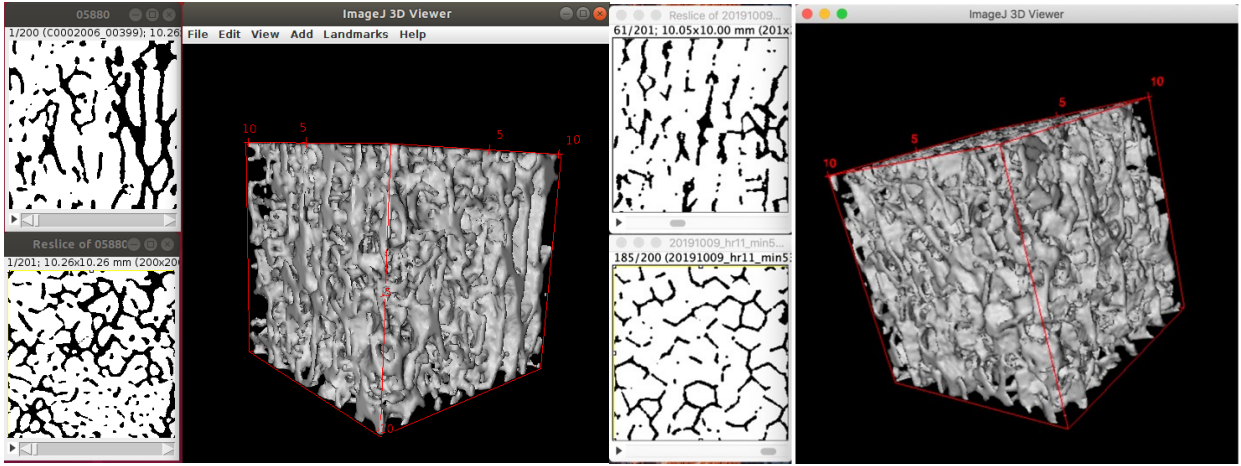


Figure 40. VOI extracted from patient 05880 (left) and corresponding simulated structure (right).

	Volume Ratio	Conn. Densit	Tb.Th Mean	Tb.Th STD	DA	Tb.Sp Mean	Tb.Sp STD
real 05880	0.2500	2.9125	0.2922	0.0970	0.2758	0.8184	0.2654
model	0.2410	2.9648	0.2225	0.0435	0.2225	0.7242	0.1686
ERROR	-3.61%	1.79%	-23.84%	-55.20%	-19.33%	-11.51%	-36.48%

Table 8. Microarchitecture measurements of the structures in Figure 40.

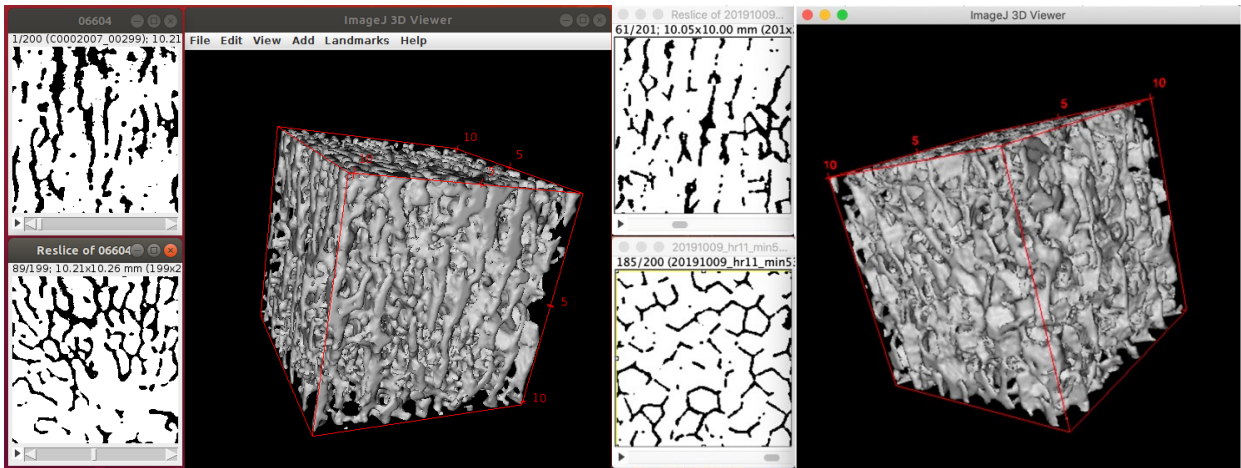


Figure 41. VOI extracted from patient 06604 (left) and corresponding simulated structure (right).

	Volume Ratio	Conn. Density	Tb.Th Mean	Tb.Th STD	DA	Tb.Sp Mean	Tb.Sp STD
real 06604	0.1906	2.9326	0.2683	0.0843	0.2486	0.8859	0.3361
model	0.1784	2.6097	0.2036	0.0417	0.2036	0.8879	0.2104
ERROR	-6.38%	-11.01%	-24.13%	-50.57%	-18.13%	0.23%	-37.40%

Table 9. Microarchitecture measurements of the structures in Figure 41.

For structure pairs from Figure 36 to Figure 41, the corresponding model is designed to match the volume ratio and trabecular spacing with the real bone structure, with BVF and Tb. Sp. as direct inputs to the model generating function. Although some of the features matched well between the real bone and the model, some of the features such as Tb.Th. and Tb. Sp. STD still showed significant deviation from the target values. Based on the relations established by the statistical analysis, modifications can be included to the model to minimize the disagreement between simulated and measured values.

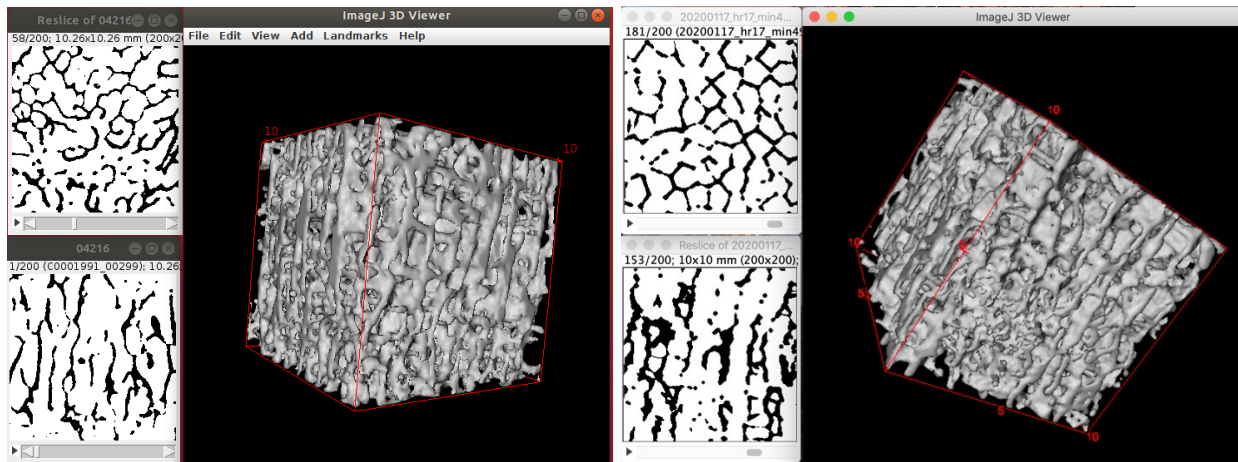


Figure 42. VOI extracted from patient 04216 (left) and corresponding simulated structure (right).

	Volume Ratio	Conn. Density	Tb.Th Mean	Tb.Th STD	DA	Tb.Sp Mean	Tb.Sp STD
real 04216	0.215119	2.6023767	0.255661	0.079225	0.27756	0.816482	0.231229
model	0.220519	2.543996	0.233935	0.043532	0.26266	0.831334	0.196103
ERROR	2.51%	-2.24%	-8.50%	-45.05%	-5.37%	1.82%	-15.19%

Table 10. Microarchitecture measurements of the structures in Figure 42.

Figure 42 (right) shows a modified version of the model corresponding to patient 04216 as shown in Figure 37. Adjustment on the input variables were made, and variations were also applied to reduce the difference in the standard deviation of trabecular thickness and spacing. Figure 42 exhibits the ability of the phantom development pipeline to generate models matching the target features.

In order to better illustrate such an ability to generate models with any target microarchitecture features, 125 of the samples were selected from the 400 human bone volumes. 125 corresponding digital phantoms were generated with similar microarchitecture features. The digital bone phantoms covered the full range of microarchitecture parameters observed from measurements on the μ CT dataset, and showed comparable parameter distribution. The mean \pm standard deviation of the parameters for human bone samples/digital phantoms were: $8.02\pm 2.21\%/9.21\pm 1.92\%$ (BVF), $0.11\pm 0.01\text{mm}/0.13\pm 0.02\text{mm}$ (Tb.th), $1.00\pm 0.18\text{mm}/0.950\pm 0.23\text{mm}$ (Tb.sp), $1.27\pm 0.06/1.30\pm 0.09$ (DA), and $3.56\pm 1.50/3.44\pm 2.31$ (Conn.D).

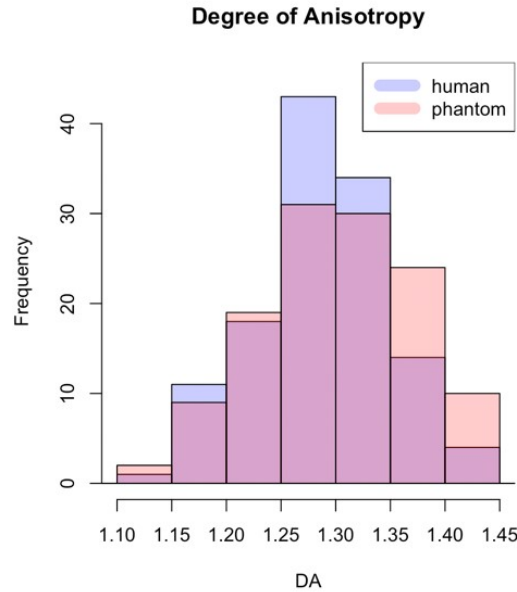


Figure 43. Histogram of degree of anisotropy to illustrate the distribution of DA of human dataset and simulated phantoms.

Mechical Properties

The mechanical properties of each structure were represented by a single value-- compressive stiffness. However, in order to provide more information on the structure, microarchitecture features are also included here. The ultimate goal of computing the physical properties is to see the difference in mechanical properties for structures with matched microarchitecture features. Table 11 shows the characteristics of four structures. Structure A, A_a, and C are real bone, and A and A_a are VOIs of the same L1 vertebral bone specimen but at sites that are next to each other, while C is extracted from another bone specimen. Structure A* is a model simulated with target microarchitecture features similar to structure A.

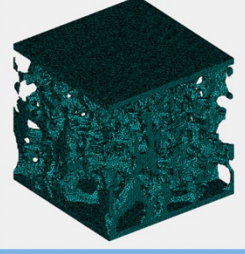
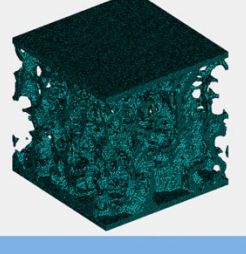
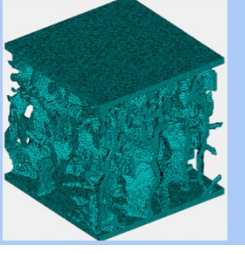
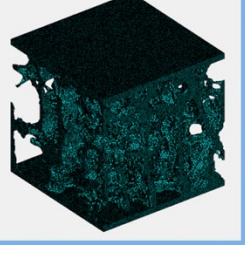
Real Bone—A (stiffness = $3.42 \times 10^3 \text{N/mm}$)			Real Bone—A_a ($3.57 \times 10^3 \text{N/mm}$)		
		A			A_a
	BVF	0.22539237		BVF	0.21732652
	Conn.D	3.08077276		Conn.D	3.00123421
	DA	0.2112557		DA	0.2023442
	Tb.Sp	0.8366814		Tb.Sp	0.8268231
	Tb.Th	0.2642167		Tb.Th	0.2462379
Model—A* (stiffness = $3.76 \times 10^3 \text{N/mm}$)			Real Bone—C ($3.97 \times 10^3 \text{N/mm}$)		
		A*			C
	BVF	0.22050865		BVF	0.26623425
	Conn.D	2.95252592		Conn.D	2.1187475
	DA	0.2462165		DA	0.28782221
	Tb.Sp	0.787691		Tb.Sp	0.8427798
	Tb.Th	0.2153367		Tb.Th	0.2827566

Table 11. Microarchitecture features and physical properties of four structures.

Table 12 shows an example of improvement on the agreement of physical properties when more variation is added to the structure, the improvement can be seen in the comparison of model_0 and model_1. As mentioned in the previous section, simulated models tend to have smaller variation throughout the volume, while real bone structure usually shows large standard deviation of trabecular spacing and thickness. Stiffness differences between the real bone and the corresponding simulated model were reduced by minimizing the difference in standard deviation of trabecular spacing and thickness.

	Volume Ratio	Conn. Density	Tb.Th Mean	Tb.Th STD	DA	Tb.Sp Mean	Tb.Sp STD	Stiffness
real 06219	0.219578125	2.7427673	0.2460251	0.0567461	0.28489672	0.9214594	0.28015385	3623
model_0	0.23050865	2.95252592	0.25533669	0.03081409	0.26621648	0.88769102	0.19698943	3952
error	4.98%	7.65%	3.78%	-45.70%	-6.56%	-3.66%	-29.69%	9.08%
	Volume Ratio	Conn. Density	Tb.Th Mean	Tb.Th STD	DA	Tb.Sp Mean	Tb.Sp STD	Stiffness
real 06219	0.219578125	2.7427673	0.2460251	0.0567461	0.28489672	0.9214594	0.28015385	3621
model_1	0.217175	2.5898298	0.256926	0.0541819	0.2741446	0.9505086	0.27947695	3490
error	-1.09%	-5.58%	4.43%	-4.52%	-3.77%	3.15%	-0.24%	-3.62%

Table 12. Improvement in the agreement of physical properties with consideration of matching standard deviation values.

Four pairs of corresponding phantom and human bone are listed in Table 13. A1, A2, A3, and A4 are real bone volumes extracted from from four individual L1 vertebral bone specimens with major difference in bone volume fraction, which is the fundamental factor contributing to mechanical strength of the bone structure. A1*, A2*, A3*, and A4* are the corresponding phantoms designed based on the microarchitecture features of the real bones with percent error on each parameter lower than 6%. For four selected pairs of corresponding phantom and human bone, the percent differences in stiffness ranged from 5.46% to 10.05%.

Figure 44 shows the physical properties illustrated as the value of Conn.D as a function of Tb.Sp. It shows that the four pairs have Conn.D and Tb.Sp. wide spread throughout the range, indicating the results are representative among the range.

	BVF(%)	Tb.Sp (mm)	Tb.Th (mm)	Conn.D (1/mm3)	DA	Stiffness (N/mm)
real bone A1	6.28	1.0488	0.1124	2.4195	1.2602	2201
phantom A1*	6.42	1.0898	0.1136	2.4959	1.2808	2338
abs %error	2.2292994	3.9092296	1.0676157	3.1576772	1.6346612	6.225869
	BVF(%)	Tb.Sp (mm)	Tb.Th (mm)	Conn.D (1/mm3)	DA	Stiffness (N/mm)
real bone A2	8.16	0.9964	0.1162	3.2741	1.2174	2473
phantom A2*	8.22	1.0001	0.115	3.4643	1.2271	2608
abs %error	0.7352941	0.3714468	1.0327022	5.80923	0.79678	5.458957
	BVF(%)	Tb.Sp (mm)	Tb.Th (mm)	Conn.D (1/mm3)	DA	Stiffness (N/mm)
real bone A3	11.53	0.764	0.1158	5.9671	1.2547	2921
phantom A3*	11.77	0.768	0.1118	6.0734	1.2033	3214
abs %error	2.0815265	0.5235602	3.4542314	1.7814349	4.0965968	10.049321
	BVF(%)	Tb.Sp (mm)	Tb.Th (mm)	Conn.D (1/mm3)	DA	Stiffness (N/mm)
real bone A4	12.73	0.8611	0.1169	6.1483	1.2317	3233
phantom A4*	12.79	0.8621	0.1189	6.4903	1.188	3527
abs %error	0.4713276	0.151263	1.710864	5.5625132	3.5479419	9.213214

Table 13. Four pairs of real bone and corresponding digital phantom.

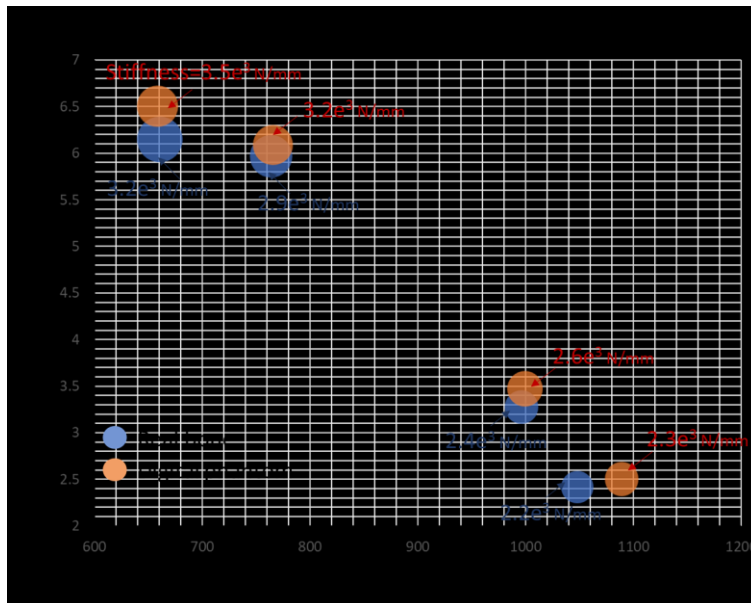


Figure 44. Visualization of the distribution of the parameters of the four pairs. Stiffness referring to force/displacement was calculated for each model. Comparison of stiffness for 4 pairs of real bone and digital phantoms generated to have matching microarchitecture (not shown on the plot) are fixed across the pairs (BVF~8.2%, Tb.Th.~115 μ m, DA~1.23).

Chapter IV

Discussions and Conclusion

Discussion of the Results

Real bone has a structure that is more diverse and with larger variation throughout the volume, whereas the simulated model was more uniform in trabecular spacing and trabecular thickness since the morphological processing of phantom generation uses a constant kernel size during dilation for the whole volume. Additionally, the real bone structure showed a more smooth curvature between the junctions of trabeculae, while the simulated model showed more abrupt turning points. Although variation was added before thresholding to increase the variation of trabecular thickness and spacing, the distribution of the seed-points determined the general structure, such that big variation in structure can hardly be seen without adding more variation during the points distributing step.

Since the microarchitecture features were not the direct input of the phantom generating program, and all the variables were affecting the output together, it was hard to obtain a structure with all target features without empirical knowledge or multiple trials. For the comparable pairs listed from Figure 29 to Figure 34, the corresponding models were designed to match the volume ratio and trabecular spacing with the real bone structures. BVF and Tb. Sp. were the direct input of the model generating function and, thus, could be easily achieved. However, as can be implied from the data, some of the features, such as Tb.Th. std and Tb. Sp. std, still exhibited significant differences between the real bone and the simulated model. Although it is possible to reach a

number that is very close to the target value, it may be too hard to make all features within 6% error in a few trials since changing one input variables may affect not only one output measurement.

The current pipeline permits the possibility to generate 3D digital bone tissue phantoms with microarchitecture features that capture the variability and complexity of human vertebral trabecular bone; however, not all combinations of the microarchitecture features can be generated as shown in Figure 32: when the BVF is small, the structure should be more porous and spacing lower than certain level was unreachable; vice versa, when the BVF is large, the structure is supposed to be denser, and large spacing is unrealistic.

The mechanical test is currently performed using Abaqus, which results in extremely long computationa time for the high resolution of the structure and the mesh considered in this study. There are more than a million tetrahedron elements in the mesh. However, the resolution cannot be decreased due to the microstructure dimension of trabecular bone. Because of the long computation time, less than 20 structures were included in the finite element analysis. The structure pairs in the result section were the ones that matched each other well both in microarchitecture and physical characteristics. The results showed that bone volume fraction contributed the most to the bone strength. For similar levels of BVF, connectivity density also played an important role on the stiffness of the structure, as more trabeculae per volume, the denser the structure is.

Although the stiffness was within a comparable range when all other microarchitecture features were matched (see Table 12), the sample size in this study was too small to establish any correlation of stiffness for any of the microarchitecture parameter alone. As a result, a strong statement stating that the digital phantom is realistic morphologically and physically cannot be drawn at the current stage. More corresponding pairs need to be included in the sample pool to

make any conclusion on the stiffness. Moreover, the human data used are patients either with osteoporosis, or at a high age; no young healthy data are included. As shown in Figure 44, the four samples have good spreadout on Tb.Sp and Conn.D, but the distribution range was defined based on human data without young healthy patients. If the bone structure of a young healthy individual has a combination of microarchitecture characteristics very different from the human data used in this study, some of the conclusions shown in the results may be not applicable to young healthy population.

Additionally, finite element analysis results rely heavily on the meshing as the fundamental of finite element analysis is to solve partial differential equations based on the meshes. In this study, tetrahedron mesh was used, but no investigation of mesh in other shape was done. The results using different meshing methods may be different. Other than that, in order to apply an uniform load onto the structure, two plates were added on the top and bottom of the structure. The two plates actually affect the microarchitecture of the structure, and the effect of the two plates will be different for different structures as the trabeculae directly connected to them are not the same. The microarchitecture features listed for each structure were not the same as the real microstructure the volume has with the added plates. However, with the same volume size, and same design of the added plates, we can assume similar effects that the plates brought to both of the structures. Although the correlation is restricted by the facts mentioned above, it indicates the microarchitecture metrics should be a partial estimate for physical property of the bone.

Conclusions

This work describes a new approach to building 3D digital bone tissue phantoms with microarchitecture features that capture the variability and complexity of human vertebral trabecular bone that includes realistic representation of microarchitecture and mechanical properties. The model established in this study can generate phantoms with the desired microarchitecture measurements within 5% error on each parameter. The capability of the designed model to generate bone structures with high variability and complexity could be a simulation tool and test method to characterize the quantitative performance of novel imaging biomarkers, as currently there is no guideline of standards on quantitative evaluation on those image-based biomarkers. Although bone quality as represented by microarchitecture features is as important as bone quantity measured by BMD in bone strength determination, it is not included in regular clinical diagnosis procedure. Hence, the novel approach provided in this study to analyze bone quality both in its characterization of bone microarchitecture and the corresponding strength can provide a more comprehensive view of bone health in the at-risk population.

A library of 3D binary vertebral trabecular phantoms for texture analysis or any other related assessments will be publicly available with coverage of a wide range of health levels of bone, in order to provide assistance to bone property characterization that is hindered by limited data. With the parametrized phantoms, ground truth--underlying microarchitecture--are included and levels of structures are well-controlled and correlated with bone strength. Therefore, these phantoms could be available for comprehensive technical assessment of quantitative measurements as the known ground truth and well-controlled levels of structures provide the possibility for bias and linearity analysis which are not always possible with actual patient data due to the availability of such data, especially for the repeatability and reproducibility analysis.

The model is highly customizable so that different microarchitecture properties can be obtained and appropriately modeled to achieve various bone health levels or trabecular bone structure at different sites.

A common application for a designed digital phantom is 3D printing. The 3D simulated phantom can be 3D printed into physical phantoms to be used in any applicable image modality. For more consistent results of microarchitecture measurements in this study, physical phantoms should be scanned by μ CT, then measurements should be done with the μ CT images to include noise level and construction artifacts which are in the real bone data. However, 3D printing materials are limited, and materials with similar imaging properties are hard to be printed in such a high resolution.

Another application is to generate simulated projection as in MDCT or other applicable image modality. Figure 46 shows a simulated projection of a complete vertebral bone specimen phantom. The internal structure of the phantom is built as the framework used in the study, and a cortical shell is added to the trabecular structure to construct a complete vertebral bone phantom as an integral. Simulated phantom can then be used to generate simulated projection to mimic MDCT/DXA image. From then, modality-based features can be extracted to do further analysis. Such a novel digital phantom development algorithm may enable discovery of new quantitative biomarkers of bone quality from modalities that are not currently common in osteoporosis diagnosis. The designed phantoms can be used to investigate the standard of level of resolution that is necessary to be reached to assess bone quality.

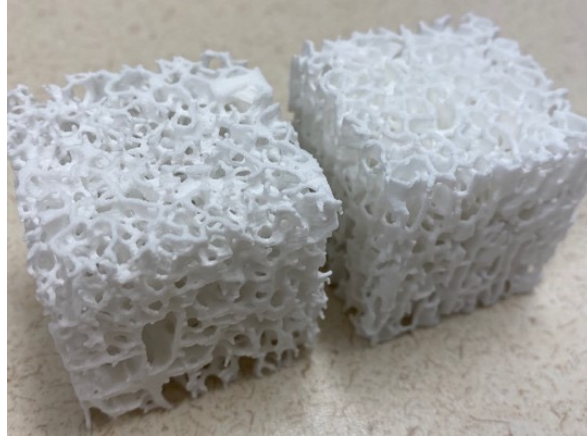


Figure 45. 3D printed bone structures of (left) real bone and (right) simulated phantom.

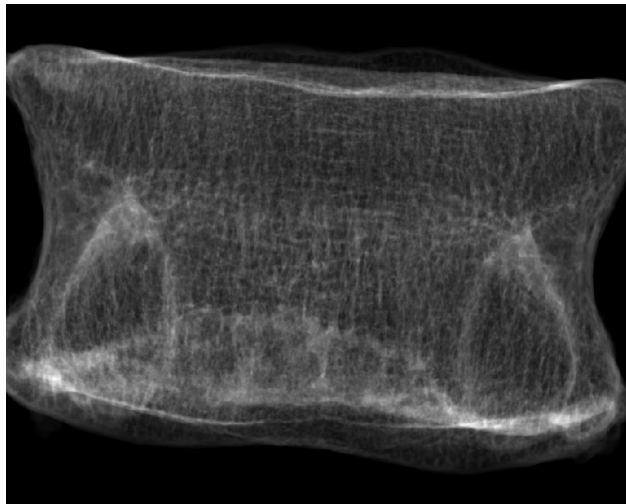


Figure 46. Simulated projection of a digital spine phantom.

Chapter V

References

Resources and References

- [1] National Osteoporosis Foundation, What is osteoporosis and what cause it? <https://www.nof.org/patients/what-is-osteoporosis/> Accessed 2017.
- [2] F. Cosman, et al., "Clinician's guide to prevention and treatment of osteoporosis", *Osteoporosis international*, **25** (2014) 2359-2381.
- [3] National Osteoporosis Foundation, What women need to know? <https://www.nof.org/preventing-fractures/general-facts/what-women-need-to-know/> Accessed 2018.
- [4] V. Gilsanz, et al., "Gender differences in vertebral sizes in adults: biomechanical implications", *Radiology*, **190** (1994) 678-682.
- [5] Y.N. Yeni, et al., "Variability of trabecular microstructure is age-, gender-, race-and anatomic site-dependent and affects stiffness and stress distribution properties of human vertebral cancellous bone", *Bone*, **49** (2011) 886-894.
- [6] F. Eckstein, et al., "Sex differences of human trabecular bone microstructure in aging are site-dependent", *Journal of Bone and Mineral Research*, **22** (2007) 817-824.
- [7] S. Amin, S. Khosla, "Sex-and age-related differences in bone microarchitecture in men relative to women assessed by high-resolution peripheral quantitative computed tomography", *Journal of osteoporosis*, **2012** (2012).

- [8] M. Hudelmaier, et al., "Gender differences in trabecular bone architecture of the distal radius assessed with magnetic resonance imaging and implications for mechanical competence", *Osteoporosis international*, **16** (2005) 1124-1133.
- [9] G. Diederichs, et al., "Assessment of trabecular bone structure of the calcaneus using multi-detector CT: correlation with microCT and biomechanical testing", *Bone*, **44** (2009) 976-983.
- [10] N. Harvey, et al., "Trabecular bone score (TBS) as a new complementary approach for osteoporosis evaluation in clinical practice", *Bone*, **78** (2015) 216-224.
- [11] M.E. Arlot, et al., "Histomorphometric and μ CT analysis of bone biopsies from postmenopausal osteoporotic women treated with strontium ranelate", *Journal of Bone and Mineral Research*, **23** (2008) 215-222.
- [12] T.M. Link, "Osteoporosis imaging: state of the art and advanced imaging", *Radiology*, **263** (2012) 3-17.
- [13] J.A. Kanis, et al., "Interpretation and use of FRAX in clinical practice", *Osteoporosis International*, **22** (2011) 2395.
- [14] B.C. Silva, et al., "Trabecular bone score: a noninvasive analytical method based upon the DXA image", *Journal of Bone and Mineral Research*, **29** (2014) 518-530.
- [15] A.J. Burghardt, et al., "Reproducibility of direct quantitative measures of cortical bone microarchitecture of the distal radius and tibia by HR-pQCT", *Bone*, **47** (2010) 519-528.
- [16] T. Lowitz, et al., "Advanced Knee Structure Analysis (AKSA): a comparison of bone mineral density and trabecular texture measurements using computed tomography and high-resolution peripheral quantitative computed tomography of human knee cadavers", *Arthritis research & therapy*, **19** (2017) 1.

- [17] P. Guggenbuhl, et al., "Reproducibility of CT-based bone texture parameters of cancellous calf bone samples: Influence of slice thickness", *European journal of radiology*, **67** (2008) 514-520.
- [18] M.R.K. Mookiah, et al., "Effect of radiation dose reduction on texture measures of trabecular bone microstructure: an in vitro study", *Journal of bone and mineral metabolism*, (2017) 1-13.
- [19] A. Valentinitich, et al., "Computational identification and quantification of trabecular microarchitecture classes by 3-D texture analysis-based clustering", *Bone*, **54** (2013) 133-140.
- [20] Q. Li, et al., "Statistical analysis of lung nodule volume measurements with CT in a large-scale phantom study", *Medical physics*, **42** (2015) 3932-3947.
- [21] Q. Li, et al., "Volumetry of low-contrast liver lesions with CT: Investigation of estimation uncertainties in a phantom study", *Medical Physics*, **43** (2016) 6608-6620.
- [22] Q. Li, et al., "Impact of reconstruction algorithms and gender-associated anatomy on coronary calcium scoring with CT: an anthropomorphic phantom study", *Academic radiology*, **23** (2016) 1470-1479.
- [23] Q. Li, et al., The effects of iterative reconstruction in CT on low-contrast liver lesion volumetry: a phantom study, in: SPIE Medical Imaging, International Society for Optics and Photonics, 2017, pp. 101340Z-101340Z-101315.
- [24] B. Ettinger, et al., "Reduction of vertebral fracture risk in postmenopausal women with osteoporosis treated with raloxifene: results from a 3-year randomized clinical trial", *Jama*, **282** (1999) 637-645.
- [25] T. Kim, et al., Mathematical network model for bone mineral density (BMD) and bone quality assessment, in: Proceedings of the 2nd ACM Conference on Bioinformatics, Computational Biology and Biomedicine, ACM, 2011, pp. 69-75.

- [26] S. Gómez, et al., "Design and properties of 3D scaffolds for bone tissue engineering", *Acta biomaterialia*, **42** (2016) 341-350.
- [27] D. Ulrich, et al., "The ability of three-dimensional structural indices to reflect mechanical aspects of trabecular bone", *Bone*, **25** (1999) 55-60.
- [28] D. Chappard, et al., "Trabecular bone microarchitecture: a review", *Morphologie*, **92** (2008) 162-170.
- [29] Warriner, Amy H, et al. "Which Fractures Are Most Attributable to Osteoporosis?" *Journal of Clinical Epidemiology*, U.S. National Library of Medicine, (2011)
- [30] Shevroja, Enisa, et al. "Use of Trabecular Bone Score (TBS) as a Complementary Approach to Dual-Energy X-Ray Absorptiometry (DXA) for Fracture Risk Assessment in Clinical Practice." *Journal of Clinical Densitometry*, Elsevier, 19 July 2017
- [31] Krug, Roland, et al. "High-Resolution Imaging Techniques for the Assessment of Osteoporosis." *Radiologic Clinics of North America*, U.S. National Library of Medicine, May 2010.
- [32] Guerra, Eliete N S, et al. "Capability of CBCT to Identify Patients with Low Bone Mineral Density: a Systematic Review." *Dento Maxillo Facial Radiology*, The British Institute of Radiology., Dec. 2017.
- [33] Tzedakis, A, et al. "The Effect of z Overscanning on Patient Effective Dose from Multidetector Helical Computed Tomography Examinations." *Medical Physics*, U.S. National Library of Medicine, June 2005.
- [34] Damilakis, John, et al. "Radiation Exposure in X-Ray-Based Imaging Techniques Used in Osteoporosis." *European Radiology*, Springer-Verlag, Nov. 2010.
- [35] Nishiyama, Kyle K, and Elizabeth Shane. "Clinical Imaging of Bone Microarchitecture with HR-PQCT." *Current Osteoporosis Reports*, U.S. National Library of Medicine, June 2013.
- [36] Du, Yue, et al. "Design and Statistical Analysis of Irregular Porous Scaffolds for Orthopedic Reconstruction Based on Voronoi Tessellation and Fabricated via Selective Laser Melting (SLM)." *Materials Chemistry and Physics*, Elsevier, 6 Aug. 2019

Curriculum Vitae

Xu Xin

925 25TH St. NW, Washington, DC
202-957-2438 | xxu63@jhu.edu

EDUCATION

- Johns Hopkins University** Baltimore, MD
MS Biomedical Engineering Sep. 2018 – May. 2020
- Biomedical Instrumentation, Medical Imaging Analysis, Computer Integrated Surgery, Medical Imaging Systems, Ultrasound and Photoacoustic Beamforming, Applied Bioelectrical Engineering, and Computation for Engineers.
- The George Washington University** Washington, DC
BS Biomedical Engineering (GPA 3.9/4.0) summa cum laude Sep. 2014 – May. 2018
- Medical Imaging, Cell Imaging, Tissue Engineering, Digital Signal Processing, MATLAB, Anatomy and Physiology, Engineering Electronics, Digital Logic, Signals and Systems, C Programming, and Engineering Analysis.
- Yonsei University** Seoul, KR
Summer Abroad Program Jun. 2016 – Aug. 2016
- Principles of Macroeconomics (A), Intermediate Korean Language 2 (A)
- University of California, Los Angeles** Los Angeles, CA
Summer Program Jun. 2013 – Aug. 2013
- Principles of Economics (A) Language & Society (B+)
- Guangdong Experimental High School** Guangzhou, CN
High School Diploma Sep. 2011 – Jun. 2014

EXPERIENCE

- U.S. Food and Drug Administration** Jul. 2019 – Present
ORISE Research Fellow
- To design a realistic computational model for vertebral trabecular bone structures and the resulting digital bone phantoms span the range of bone health level from healthy to osteoporotic state, with known ground truth of bone microarchitecture parameters.
 - To create 3D printed trabecular bone phantoms and a library of public CT datasets for use in the development and assessment of relevant CT-based fracture risk prediction tools and biomarkers.
 - To assess the quantitative performance of simulated model by comparing to real bone samples from public database using finite element analysis on physical properties and microarchitecture analysis on structure measurements.
 - Work as an FDA fellow to attend and assist internal and public events to promote Division of Imaging, Diagnostics, and Software Reliability (DIDSR) of FDA.
- Neuroengineering and Biomedical Instrumentation Laboratory** Sep. 2018 – May. 2019
Research Assistant
- Responsible for data management, including data transformation, data storage, and data maintenance.
 - Improved MATLAB algorithm to acquire quantitative information of EEG signal by denoising original signal and developed potential quantitative biomarker for brain active level.
 - Designed MATLAB algorithm to quantify relationship between EEG and neurovascular coupling.
 - Work in team with surgery doctors, imaging technicians, and Laser Speckle Contrast Imaging analysts to have comprehensive understanding on the surgery protocol and physiological grounds of the project.
- Breast Oncology Research Center, GW Medical Faculty Associate** Sep. 2017 – May. 2018
Clinic Assistant
- Assist infrared thermography imaging process with patients at MFA breast clinic.
 - Designed the setup of a supplementary infrared reflective mirror of the patient chair in order to obtain the breast side view in the clinic.
 - Responsible for equipment set up, imaging and communicating procedure to patients.
- Laboratory for Medical Imaging and Image Analysis** Jun. 2017 – May. 2018
Research Assistant
- Designed MATLAB algorithm for automated image segmentation of breast region and pixel intensity analysis of the infrared images to increase computational efficiency and remove signal interference.

ADDITIONAL PROJECTS

- Designed MATLAB GUI tool for analyzing ECG changes during the progression of cardiac activities to provide clinical suggestion on CPR/defibrillation under ER situation. The MATLAB GUI consists of following capabilities: Amplitude Spectrum Area (AMSA) calculation, Fast Fourier Transform of the signal, high and low pass filters, moving and triangle average filter, heart rate variability calculation, and overall conclusion based on all measurements. **Single recipient of the Best Senior Design Award.**
- Designed and built a **portable frog heart rate monitor** which includes a 3D fabricated portable container and ECG detecting circuit as hardware, and ECG monitoring application as software.
- **Recovery of complete dataset** of ultrasound raw signals from focused transmit beams to achieve improved focusing and contrast at every focal depth using MATLAB.
- Designed and built a **smart cane** for blind integrating C++ micro-controllers and circuits. The smart cane is capable to assist user in distinguishing various types of obstacle.
- Designed and built a **wearable device** to alert unhealthy gait posture integrating C++ micro-controllers and circuits.
- Built a **therapy toy** for autistic children integrating C++ micro-controllers and circuits, included 3D printed parts.
- MATLAB programmed Dual Tone Multiple Frequency signal encoding and decoding system.
- Programmed a **device that stores patient's OCT image data** of the lining of the bladder, sorts them using a binary search tree based on the diagnosis as well as a linked list using C.

AWARDS

The Best Senior Design Award

2018

- This award is given to best senior project within Department of Biomedical Engineering.

Dean's List (received 4 years)

2015, 2016, 2017, 2018

- This award is given to undergraduate who has 30 credits or more in any one semester, earns 12 credits or more and attain a minimum semester grade point average of 3.75 in letter-graded coursework.

GWU Outstanding Academic Achievement Award

2016

- Each year the George Washington University recognizes dedication to excellence in learning by honoring the Outstanding Academic Achievement Award Recipients, the top 2% by GPA, who have distinguished themselves inside and outside the classroom.

COMPUTER SKILLS / ASSETS

MATLAB:

- Learned within curriculum. Circuits, signals, and systems; Digital Signal Processing; Cell Imaging; Image Analysis; Computation for Engineers; Ultrasound and Photoacoustic Beamforming.
- Undergraduate Senior Design on clinical biomarker for ventricular fibrillation in ER environment using MATLAB.
- Master's project on 3D digital trabecular bone structure analysis and modeling developed using MATLAB.

C/C++:

- Learned within curriculum: C Programming for ECE; BME Programming II; Biomedical Instrumentation.
- Programmed a micro controller which detects force distribution and provides corresponding feedback.
- Programmed a micro controller which rotates an ultrasound sensor and an IR sensor to detect and alert obstacle within certain range.

R:

- Statistical analysis for master's dissertation project of digital 3D bone structure model development.

Abaqus:

- Finite element analysis for bone structure of simulated digital bone phantoms and real bone samples.

Image J:

- Micro-CT image processing and analysis for bone microarchitecture feature extraction.

Solidworks:

- CAD design for gears and wheels used in therapeutic toy project
- 3D meshing and 3D printing model of simulated vertebral trabecular bone phantoms.

Verilog:

- Programmed a digital door lock using Digital Logic Xilinx ISE Design Suite 13.2 and Basys Board.

TECHNICAL SKILLS

SCANCO Micro-CT Scanner, Infrared Camera; Agilent E3631A (DC Power Supply), Keithley 175 Digital Multimeter (DMM), Agilent 34460A, Digital Multimeter (DMM), Agilent DSO1024A Digital Oscilloscope, Agilent 33522 A Function/Arbitrary Waveform Generator, UFI 2122 BioAmplifier.

LANGUAGE SKILLS

English: Bilingual Proficiency
Cantonese: Bilingual Proficiency

Mandarin: Bilingual Proficiency
Korean: Professional Working Proficiency